Mineralogy and temperature of crater Haulani on Ceres

F. TOSI [1*], F. G. CARROZZO[1], A. RAPONI[1], M. C. DE SANCTIS [1], G. THANGJAM [2],
F. ZAMBON[1], M. CIARNIELLO[1], A. NATHUES[2], M. T. CAPRIA[1], E. ROGNINI[1],
E. AMMANNITO[1,3], M. HOFFMANN[2], K. KROHN[4], A. LONGOBARDO[1], E. PALOMBA[1],
C. M. PIETERS [5], K. STEPHAN [4], C. A. RAYMOND[6], and C. T. RUSSELL[7]

[1]Istituto Nazionale di Astrofisica, Istituto di Astrofisica e Planetologia Spaziali (INAF-IAPS), Via del Fosso del Cavaliere 100,
I-00133 Rome, Italy
[2]Max Planck Institute for Solar System Research, Justus-von-Liebig-Weg 3, D-37077 Göttingen, Germany
[3]Italian Space Agency (ASI), Via del Politecnico snc, I-00133 Rome, Italy
[4]Institute of Planetary Research, German Aerospace Center (DLR), Rutherfordstrasse 2, D-12489 Berlin, Germany
[5]Department of Earth, Environmental and Planetary Sciences, Brown University, 324 Brook Street, Providence, Rhode Island
02912, USA
[6]NASA/Jet Propulsion Laboratory and California Institute of Technology, 4800 Oak Grove Drive, Pasadena,
California 91109, USA
[7]Institute of Geophysics and Planetary Physics, University of California at Los Angeles, 3845 Slichter Hall, 603 Charles E.
Young Drive, East, Los Angeles, California 90095–1567, USA
[*]Corresponding author. E-mail: federico.tosi@iaps.inaf.it

(Received 05 July 2017; revision accepted 28 February 2018)

Abstract–We investigate the region of crater Haulani on Ceres with an emphasis on mineralogy as inferred from data obtained by Dawn's Visible InfraRed mapping spectrometer (VIR), combined with multispectral image products from the Dawn Framing Camera (FC) so as to enable a clear correlation with specific geologic features. Haulani, which is one of the youngest craters on Ceres, exhibits a peculiar "blue" visible to near-infrared spectral slope, and has distinct color properties as seen in multispectral composite images. In this paper, we investigate a number of spectral indices: reflectance; spectral slopes; abundance of Mg-bearing and NH_4-bearing phyllosilicates; nature and abundance of carbonates, which are diagnostic of the overall crater mineralogy; plus a temperature map that highlights the major thermal anomaly found on Ceres. In addition, for the first time we quantify the abundances of several spectral endmembers by using VIR data obtained at the highest pixel resolution (~0.1 km). The overall picture we get from all these evidences, in particular the abundance of Na- and hydrous Na-carbonates at specific locations, confirms the young age of Haulani from a mineralogical viewpoint, and suggests that the dehydration of Na-carbonates in the anhydrous form Na_2CO_3 may be still ongoing.

INTRODUCTION

The 34 km crater Haulani is one of the youngest surface features on the dwarf planet Ceres. This crater is centered at 5.8°N, 10.77°E, and gives the name to quadrangle Ac-H-6 "Haulani" (Lon 0°–72°E, Lat 22°S–22°N), one out of five quadrangles that cover the equatorial region of Ceres (Roatsch et al. 2016). Crater Haulani, which is the fourth largest crater within quadrangle Ac-H-6, is a distinct geologic unit in itself, being made up by a complex patchwork of subunits of varying extents. Haulani formed on the transition between a central plateau in the east and a topographic low in the west (Krohn et al. 2016, 2017). It exhibits interior smooth plains with flow features originating from a hummocky elongated mountainous ridge in the center, ponding toward mass-wasting deposits of the rim. Several flow features are observed running from the crater rim outward to the surrounding area, covering the pre-existing surface (Krohn et al. 2016).

The smooth crater floor is laced by pits. Some pit crater chains in the northwestern part are oriented parallel to the rim (Krohn et al. 2016; Sizemore et al. 2017). Most notable geologic units mapped within crater Haulani are: bright lobate material (lb), knobby bright lobate material (lkb), smooth lobate material (ls), and smooth bright lobate material (lsb). Haulani's bright ejecta (crb) is widespread over the cerean surface, preferentially to the west, extending into quadrangle Ac-H-10 "Rongo" (Platz et al. 2017; Zambon et al. 2017b).

High albedo, blue spectral slope, and physical smoothness all appear to be indicators of youth (Schröder et al. 2017). Crater Haulani shows strong bluish characteristics and appears to be relatively young based on its pristine morphology. Due to its youthful nature, the number of craters superimposed on their ejecta blankets is relatively small. Measurement areas in the proximity of crater Haulani provide an age overall comprised between 1.7 and 5.9 Myr (Schmedemann et al. 2016), depending on whether the LDM (lunar-derived model) (Schmedemann et al. 2014; Hiesinger et al. 2016) or ADM (asteroid-derived model) (O'Brien et al. 2014; Hiesinger et al. 2016) chronology systems are applied.

While the average reflectance spectrum of Ceres lacks distinctive features in the spectral range 1.0–2.5 µm, the thermally corrected wavelength region 2.6–4.2 µm as explored by VIR in the early Survey orbit phase, which lasted from June 5, 2015 to June 30, 2015 and obtained nearly global hyperspectral coverage at ~1.1 km/px, displays a broad asymmetric feature, characteristic of H_2O/OH-bearing materials. Within this broad absorption are several distinct absorption bands, centered respectively at 2.72–2.73 µm, 3.05–3.1 µm, 3.3–3.5 µm, and 3.95 µm (De Sanctis et al. 2015). The 2.72–2.73 µm feature is distinctive for OH-bearing minerals. This prominent band is best fitted by a mixture including Mg-bearing phyllosilicates such as Mg-serpentine (antigorite) (Ammannito et al. 2016). NH_4-bearing minerals, such as NH_4-serpentines and NH_4-smectites, show clear absorptions at 3.05–3.1 µm and at 3.3 µm (Bishop et al. 2002; Ehlmann et al. 2018), whereas the 3.3–3.5 µm feature, when observed in conjunction with a 3.95–4.0 µm absorption band, has been definitively attributed to carbonates (Rivkin et al. 2006; De Sanctis et al. 2015). The 3.95–4.0 µm carbonate band position is diagnostic of the carbonate composition, with an average band center (BC) value of 3.947 µm indicative of Mg or Mg-Ca carbonates (e.g., magnesite, $MgCO_3$, or dolomite, $MgCa(CO_3)_2$), and a few recognizable km-size areas displaying BCs at longer wavelengths, up to 4.02 µm, consistent with natrite (Na_2CO_3) (Carrozzo et al. 2018). These lithologies, plus a spectrally featureless dark material yet to be identified, which is actually the most abundant spectral
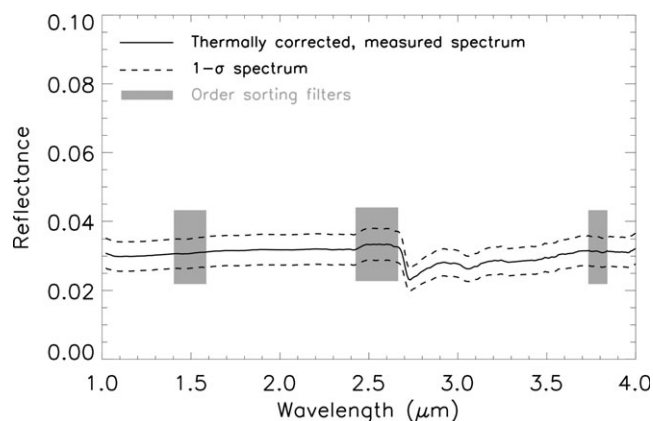

Fig. 1. Average spectrum of Ceres in the $25° \times 25°$ region roughly centered on crater Haulani, as measured by the VIR imaging spectrometer in the 1–4 µm spectral range during the HAMO mission phase at an average resolution of 0.38 km/px. The solid line represents the mean spectrum, while the dashed lines mark the 1-σ variability. All VIR spectra used to compute the average spectrum were first corrected for thermal emission, and then for illumination and observation geometry by means of a Hapke's model. Gray boxes highlight the spectral counterparts (position and width) of three-order sorting filters placed on top of the VIR infrared focal plane, which induce systematic artifacts in VIR spectra. The spectral signatures diagnostic of Mg-bearing phyllosilicates and NH_4-bearing phyllosilicates are centered at 2.72–2.73 µm and 3.06 µm, respectively. The carbonates' signatures, at 3.3–3.5 µm and 3.95–4.02 µm, are much weaker compared to the previous features.

endmember, are ubiquitous at ~1 km spatial resolution (Ammannito et al. 2016; Carrozzo et al. 2018). The identification of the dark endmember is challenging because its spectrum is essentially featureless, except for a tentative absorption band centered at 1 µm, which in principle may be attributed to iron (Fe). While magnetite (Fe_3O_4) provides a good spectral match, a large amount of Fe is inconsistent with GRaND measurements (Prettyman et al. 2017). Because CI and CM carbonaceous chondrites are the meteoritic analogs closest to the average reflectance spectrum of Ceres (Chapman and Salisbury 1973), the dark endmember is very likely carbon-bearing material.

Figure 1 shows an average reflectance spectrum of the $25° \times 25°$ area covering crater Haulani, on which our paper focuses, as measured by VIR in the near-infrared range 1–4 µm and during the High Altitude Mapping Orbit (HAMO) mission phase (~0.38 km/px). In this average spectral profile, the main absorptions so far described can be identified.

On Ceres, some peculiar surface compositions can be found at the local scale. Cerealia Facula, i.e., the very bright unit in the center of the 92 km crater Occator, is especially rich in anhydrous sodium carbonate (natrite), and it appears to represent the most concentrated known

occurrence of km-scale carbonates beyond the Earth (De Sanctis et al. 2016). The northern flanks of Ahuna Mons, the highest mountain on Ceres, also display a larger amount of Ca-carbonates and Na-carbonates compared to surrounding regions (Zambon et al. 2017a). Water-ice–rich units mixed with low-albedo components were discovered only in about 10 specific places at the surface, at latitudes poleward of 30° in fresh craters near rim shadows (Combe et al. 2016, 2017; Nathues et al. 2017; Stephan et al. 2017; Raponi et al. 2018b) and at some permanently shadowed craters (Platz et al. 2016). Furthermore, aliphatic organic matter was found to be mainly localized on a broad region of ~1000 km^2 close to the ~50 km Ernutet crater (De Sanctis et al. 2017, 2018; Pieters et al. 2018).

Unlike previous work describing the mineralogy of the quadrangle Ac-H-6 "Haulani" as a whole (Tosi et al. 2017), here we focus on a 25° by 25° area located between Lat 7°S–18°N and Lon 0°–25°E and roughly centered on crater Haulani, describing its mineralogy in detail with the goal of shedding light on the physical processes that may have led to today's observational evidences, and presenting one scenario that could explain the observed mineralogy. Such an analysis can ultimately help us reconstruct the history of this region; e.g., phase change of volatile-rich upper crust of Ceres upon impact, followed by mobilization from impact-induced heating and fluidization of crustal material, followed by equilibrium dehydration upon exposure to the surface of Ceres.

TOOLS AND TECHNIQUES

We rely on two data sets acquired by the remote sensing instruments onboard NASA's Dawn spacecraft, which entered orbit around Ceres in March 2015 (Russell et al. 2016). The first data set is optical imagery acquired by the Framing Camera (FC) (Sierks et al. 2011), and the second data set is hyperspectral data acquired by the Visible InfraRed mapping spectrometer (VIR) in the overall spectral range from 0.25 to 5.1 μm (De Sanctis et al. 2011). In both cases, our analysis is largely based on data acquired in the HAMO mission phase, which took place between August 18, 2015 and October 22, 2015, yielding an average spatial resolution of ~0.38 km for VIR and ~0.14 km for FC.

Mineralogical tools used in this work are: color composite maps, reflectance measured at specific wavelengths unaffected by known or expected spectral signatures (therefore representative of the spectral continuum), spectral slopes, BC, and band depth (BD).

A spectral slope is measured by interpolating the spectral profile between two given wavelengths with a linear fit. In both the visible and near-infrared spectral ranges, spectral slopes may be due to a number of causes: composition (e.g., presence of water ice, anhydrous salts, organics, or nanophase iron particles), dessication (Poch et al. 2016), grain size (e.g., Cloutis et al. 2012; Binzel et al. 2015), and age of the surface regolith (e.g., Riner and Lucey 2012), therefore highlighting both the chemico-physical state and space weathering processes.

BC and BD are typical spectral parameters used both in laboratory spectra and in remotely sensed spectral data sets to reveal the mineralogical composition of a planetary surface and the physical characteristics of the regolith (e.g., Clark and Roush 1984; Clark 1999). The BC is the location of the reflectance minimum inside the band after spectral continuum removal. The analysis of the BC for the main diagnostic spectral signatures seen in the infrared spectrum of Ceres shows that it does not change significantly for Mg- and NH$_4$-bearing phyllosilicates (Ammannito et al. 2016), whereas it can change for carbonate minerals, where an increase in the BC value from 3.95 to 4.02 μm is indicative of a smooth transition between Mg- or (Mg,Ca)-rich carbonates and Na-rich carbonates (Palomba et al. 2017; Carrozzo et al. 2018). In this regard, Na- and Mg-Ca carbonates are thought to originate in aqueous environments in the subsurface of Ceres, where the liquid was relatively alkaline and should have contained a large fraction of chlorides and alkali/alkaline elements. Hydrated Na-carbonates could form early in a global ocean in equilibrium with the altered rocky phase and be incorporated in Ceres's crust upon freezing of that ocean (Carrozzo et al. 2018).

The BD is defined, after Clark and Roush (1984), as: $D_B = (R_C - R_B)/R_C$, where R_B and R_C are the reflectance of the band and the spectral continuum at the BC. BDs are indicative of a mineral's abundance, the presence of opaque minerals or other phases, and may also depend on the grain size distribution (e.g., Adams 1974; Clark 1999). In general, the presence of opaque minerals tends to reduce or even suppress an absorption band, depending on the thickness of the absorbing layer. Unlike BCs, BD values are affected by illumination and observation geometry, hence a photometric correction is required to allow a proper evaluation of this parameter. In this regard, Ciarniello et al. (2017) applied Hapke's model to the VIR data set obtained at Ceres in the early mission stages, i.e., Survey and pre-Survey approach phases yielding a spatial resolution >1 km/px, to perform a photometric correction to standard observation geometry (solar incidence angle $i = 30°$, emission angle $e = 0°$, and solar phase angle $\alpha = 30°$) at VIS-IR wavelength. This resulted in VIR-derived reflectance maps and color

maps of the surface. We applied the same procedure to HAMO data, in order to allow proper estimation of BD values also for that data set, which was used to produce the spectral maps described later in this paper.

VIR-derived maps were computed from hyperspectral images acquired in the HAMO phase, and interpolated on a 1000×1000 pixel grid, i.e., with a resolution of 40 px/deg. The mineralogical maps on which our analysis dwells are based on the BDs of the 2.72–2.73 μm (hereafter 2.7 μm) and 3.05–3.1 μm (hereafter 3.1 μm), plus the BC and BD of the 3.95–4.02 μm (hereafter 4.0 μm) spectral features. Stripes and spurious values, which are identified as artifacts in the data, were first removed by using the procedure described in Carrozzo et al. (2016), then each spectrum in units of calibrated radiance factor (I/F) was corrected for thermal emission in the spectral range 1.0–4.2 μm following the method described in section 3 of Raponi et al. (2018a). Briefly, the total radiance is modeled by accounting for both the contributions of the reflected sunlight (solar spectrum scaled to the heliocentric distance and modeled by a photometric function in such a way that the surface topography and/or the photometric characteristics of the surface can be taken into account) and the thermal emission (in turn given by the product of effective emissivity and a Planck function). The estimation of the thermal emission to be removed is done simultaneously with the reflectance modeling, in order to yield a consistent result between these two contributions to the total signal measured. The error introduced by the thermal removal is estimated by calculating the standard deviation σ of the reflectance at 3.65 μm from several random pixels. The resulting $\sigma_{3.65\ \mu m}$ is compatible with the $\sigma_{1.2\ \mu m}$ calculated from the same pixels at 1.2 μm, thus outside the thermal emission region, thus ruling out any significant noise introduced by the thermal emission removal. Finally, the photometric correction mentioned in the previous section (Ciarniello et al. 2017) was applied to thermally corrected spectra. Although a few residual artifacts may still show up after this postprocessing, further analysis can eventually exclude those hyperspectral images or specific values that are not spatially coherent or are clearly the counterpart of spurious instrumental artifacts.

The long-wavelength range of VIR sensitivity, 4.5–5.1 μm, is used to systematically retrieve surface temperatures with the method described in the appendix of Tosi et al. (2014), which is a Bayesian approach to nonlinear inversion. Briefly, a synthetic radiance spectrum is computed by summing the solar contribution and the thermal contribution, with emissivity and temperature defined by their respective first guesses. The Kirchhoff's law is used to relate reflectance with emissivity. This is a two-step process: in the first step, spectral emissivity and temperature providing the best fit with the measured spectral radiance within the instrumental error in the 4.5–5.1 μm range (where thermal emission is predominant on most of the dayside) are iteratively and simultaneously computed in a cycle, until convergence around stable values is achieved. In the second step, the scalar value of the surface temperature is retained and a second Bayesian retrieval is performed by considering a broader spectral range starting 0.5 μm shortward of the crossover point to compute the spectral emissivity up to the upper bound of VIR sensitivity (5.1 μm).

Formal errors on the unknown quantities, related to random variations of the signal, are also a standard output of the Bayesian algorithm: each temperature image of Ceres can be associated to an image of the formal errors on the retrieved values, and similarly, for each wavelength where emissivity is retrieved, there is an associated uncertainty. VIR is not sensitive to physical temperatures on the nightside of Ceres, where the signal from the target is considerably low. In VIR data acquired at Ceres, uncertainties increase with decreasing surface temperature, and 170–180 K is the typical minimum temperature value that can still be retrieved while keeping uncertainties <30 K (typical uncertainties are <1 K for temperature values >200 K).

These data were used both to produce global maps and to investigate in detail the behavior of local-scale features. The motivation for our investigation is the search for thermal anomalies, that is, regions whose response to insolation differs from the average behavior of the quadrangle and of the dwarf planet as a whole. The surface of Ceres is expected to have a low thermal inertia at global and broadly regional scale (Hayne and Aharonson 2015; Titus 2015), but departures from this behavior may be found at the local scale, e.g., due to variations in regolith thickness, density (also in terms of coarser grain size, well beyond the resolution of FC images), or thermal conductivity. For this reason, we also include a map of surface temperature of the region of crater Haulani derived from VIR infrared data.

To further investigate the composition of the Haulani crater region, we applied spectral unmixing to VIR data, with the goal of estimating abundances of minerals known or expected to exist in this area (for an up-to-date overview of spectral unmixing applied to hyperspectral data sets, the uninitiated reader can look at Dalla Mura et al. 2014; Dobigeon et al. 2016; Rand et al. 2017). This analysis is the main point of novelty compared to previous works that have so far dealt with the Haulani region. For this purpose, we used VIR data acquired in the Low Altitude Mapping Orbit (LAMO) mission phase, which lasted from December 16, 2015

until August 8, 2016, yielding an average VIR pixel resolution of ~0.095 km. Unlike the Survey and HAMO phases, LAMO data coverage is much sparser with respect to global coverage, which is why LAMO data are used to characterize only specific features observed at the local scale, rather than to build spectral maps of broader regions.

In the framework of VIR data analysis, linear spectral unmixing techniques had been used in the past for specific material units or regions of interest (ROI) on Vesta (Tosi et al. 2015b; Zambon et al. 2016). However, in that case the linear approach was first validated on laboratory-derived spectral endmembers selected a priori and then applied to remotely sensed VIR data. This time, we selected a number of spectral endmembers and used a nonlinear spectral mixing method, whose details are provided in section 5 of Raponi et al. (2018a). In each hyperspectral image, VIR spectra were extracted in the range 1.0–4.2 μm, which is diagnostic of the main lithologies found on Ceres and offers at the same time a reliable responsivity and higher signal-to-noise ratio (SNR). These spectra were modeled as an intimate mixture of different endmembers using Hapke's radiative transfer model (Hapke 1993, 2012), which characterizes light scattering in particulate media. In Hapke's model, the reflectance spectrum of a regolith is computed linearly from the single-scattering albedos (SSA) of mineral endmembers. The SSA is the probability that a photon incident on a regolith particle will be scattered rather than absorbed. This parameter is independent of illumination or viewing geometry, whereas it is a function of a grain's scattering behavior and absorption coefficient. The absorption coefficient is governed by the material's complex index of refraction, which is a function of the optical constants. Optical constants are wavelength-dependent quantities unique to each particle type in a regolith and represent the inherent physical and chemical properties of each material.

We used a total of 10 spectral endmembers, whose details are reported in Table 3. They are (1) Kerite (solid bitumen); (2) Water ice (areal mixing); (3) Dark, spectrally featureless material (e.g., magnetite); (4) NH_4-montmorillonite; (5) NH_4Cl; (6) Antigorite (Mg-bearing phyllosilicate); (7) Illite (Al-bearing phyllosilicate); (8) Dolomite ($MgCa(CO_3)_2$); (9) Natrite (Na_2CO_3); and (10) Hydrous natrite ($NaHCO_3$). These endmembers were chosen so as to be representative of the average mineralogy of Ceres (De Sanctis et al. 2015, 2018; Ammannito et al. 2016) and of specific surface features known to be enriched in sodium carbonates and NH_4-salts (De Sanctis et al. 2016; Carrozzo et al. 2018; Zambon et al. 2017a), such as Cerealia Facula in the middle of crater Occator, or enriched in organics similar to those discovered in the region of crater Ernutet (De Sanctis et al. 2017; Pieters et al. 2018), as well as to investigate the possible presence of water ice, albeit ice and hydrated minerals are unlikely at such low latitudes (e.g., Bu et al. 2018). Although in the Introduction we have clarified that magnetite cannot be mainly responsible for the dark material that is most abundant on the surface of Ceres, carbonaceous chondrite being a more reasonable endmember, here what matters is the spectral profile, which does not change significantly using this endmember or a carbonaceous chondrite. The optical constants were derived from reflectance spectra as in Carli et al. (2014), except for water ice (Warren 1984; Mastrapa et al. 2008, 2009; Clark et al. 2012). The SSA is modeled starting from these mineral endmembers.

Volumetric abundances and grain sizes (assumed equal for all endmembers) are the main outputs of the model. The best-fitting result is obtained by comparison of the model with the measured spectra, applying the Levenberg–Marquardt method for nonlinear least-squares multiple regression (Marquardt 1963). The model accounts for the viewing geometry (incidence, emission, and phase angle), which is calculated according to the shape model, the spacecraft attitude, and the latitude and longitude of a given pixel on the surface. The model also accounts for the single particle phase function, which is a free parameter in the fitting procedure. In general, abundances <1 vol% can be considered negligible, because they do not provide any meaningful contribution in achieving a best fit.

GENERAL MINERALOGY OF CRATER HAULANI

Reflectance, Colors, Topography, and Spectra from FC Data

From the FC-derived clear-filter reflectance mosaic (Fig. 2a), photometrically corrected by applying a phase angle-dependent brightness function (Roatsch et al. 2016), bright and dark materials stand out in the region of crater Haulani, as having substantially higher or lower reflectances than the quadrangle's average value of 0.03 (Tosi et al. 2017). Overall, crater Haulani is one of the brightest features on Ceres, with its bright interior and its prominent ejecta with far-ranging crater rays (Krohn et al. 2017). The high albedo of the Haulani area was first recognized in Hubble Space Telescope images (Li et al. 2006) and then relocated in Dawn FC Approach and Survey images (Li et al. 2016). Bright material units within Haulani, corresponding to the central mound and to outcrops found in the western inner wall close to the rim, reach a maximum reflectance value of 0.05 in Fig. 2a. While these are

Fig. 2. a) Reflectance map of the region of crater Haulani, obtained through photometric correction of FC clear-filter data acquired in the HAMO mission phase. The map scale is ~140 m/px. b) Geologic map of crater Haulani, adapted from Krohn et al. (2017). A legend placed to the right of the map explains the meaning of the different colors. c) *RGB* composite of crater Haulani made from FC color ratios: *R*: 0.75/0.44 μm; *G*: 0.75/0.92 μm; *B*: 0.44/0.75 μm ("Clementine" color composite). Color ratios may highlight differences in material and composition. d) *RGB* composite of crater Haulani made from FC colors: *R*: 0.96 μm; *G*: 0.75 μm; *B*: 0.44 μm ("enhanced" color composite). Compared to the Clementine presentation, this color scheme enhances differences in albedo. e) *RGB* composite of crater Haulani showing spectral slope calculated between 0.555 and 0.829 μm. f) Portion of the digital terrain model (DTM) derived from FC images acquired in HAMO, at a scale of 60 px/deg. The color palette follows height in km with respect to the reference ellipsoid (i.e., the curvature of the body is removed), with the highest elevations in brown and the lowest terrains in magenta/white. (Color figure can be viewed at wileyonlinelibrary.com.)

small values in absolute terms, the variation with respect to the average value is as large as 60%. In maps of normal albedo, Haulani's brightest material reaches a maximum value of 0.12, which is lower than Cerealia Facula (the brightest feature on Ceres, located in the center of crater Occator) but comparable to Ahuna Mons (0.13–0.14) and crater Kupalo (0.13) (Schröder et al. 2017). However, to avoid confusion in the quantities that describe the brightness of the features on which our analysis focuses, in most of this paper we will use reflectance rather than albedo.

Geologic mapping (Fig. 2b, adapted from Krohn et al. 2017) established that, among bright units found in Haulani, knobby bright lobate material (lkb) extends around the northern and eastern crater rim, and smooth bright lobate material (lsb) only occurs as smaller branches in the south-southeast and north-northeast, covering the surface with streaky flow-like material. Particularly prominent is a bright lobate material (lb), extending westward. This material shows a relatively smooth surface with many flow fronts. Crater floor hummocky bright material (cfhb) also occurs only in Haulani crater and shows a high reflectance. Smooth crater floor material (cfs) has a very smooth surface without craters, only a few pits are visible, as well as some cracks and pit crater chains, with visible reflectance a bit darker than the surroundings, and a bluish to brownish color in FC enhanced color mosaics (see below). Smooth dark crater floor material (cfsd) also shows the same morphological characteristics as cfs, but additionally contains a lot of pits and some channels and is deposited topographically higher in Haulani crater. The reflectance is significantly darker than the surrounding areas, and the enhanced color mosaic shows a dark blue color. Compared to the other crater floor material smooth units, bright smooth crater floor material (cfsb) indeed has similar morphological characteristics, but no linear features are visible and the reflectance is significantly higher than the surroundings. Finally, bright crater ray material (crb) deposits occur as bright streaks or radial halos around the Haulani impact crater and cover the adjacent terrain with a somewhat thin layer. This unit exhibits a high

reflectance compared to the surrounding terrain in FC clear-filter images.

In the so-called "Clementine" color presentation (*R*: 0.75/0.44 μm, *G*: 0.75/0.92 μm, *B*: 0.44/0.75 μm, Pieters et al. 1994), which was found to be a useful way to emphasize color variations on the Moon and on the large asteroid Vesta, most of the Ceres surface is reddish (*R*: 1.074, *G*: 1.022, *B*: 0.931) (Fig. 2c), while crater Haulani is the most prominent multispectral unit, displaying an overall light blue color, with bright crater ray material appearing cyan (*R*: 0.921, *G*: 1.068, *B*: 1.086) and the brightest units in the crater's floor displaying a slightly greenish shade (*R*: 0.936, *G*: 1.067, *B*: 1.069). However, the southeastern inner wall of Haulani, and smaller patches close to the northern rim, which may represent redeposited slumping material from the southern topographic heights (Stephan et al. 2017), retain the red color (*R*: 1.096, *G*: 0.993, *B*: 0.912) typical of the rest of the quadrangle.

A second color scheme, which is more suited to Ceres, is the "enhanced" color composite (*R*: 0.96 μm, *G*: 0.75 μm, *B*: 0.44 μm), displayed in Fig. 2d. In this presentation, most of the surface on Ceres has a brownish color (*R*: 0.029, *G*: 0.030, *B*: 0.028), while crater Haulani remains the most prominent multispectral unit, with ejecta material displaying a typical bluish color (*R*: 0.031–0.032, *G*: 0.034–0.035, *B*: 0.037–0.038). Compared to the "Clementine" presentation, this color scheme shows many more color shades and enhances differences in reflectance, with bright materials concentrated particularly in the Haulani crater's floor appearing whitish (*R*: 0.038, *G*: 0.042, *B*: 0.045), while dark material units of smaller areal extent appear dark blue to violet (*R*: 0.028, *G*: 0.030, *B*: 0.033). Subtle differences can be noticed in the southeastern inner wall of Haulani as well as other smaller patches located just below its northern rim, when using this color scheme compared to the Clementine color scheme. However, the latter still makes sense to be shown, because the blue ejecta of Haulani, standing out against a generally red background, are more contrasted than in the "enhanced" presentation, making it easier to follow them at increasingly larger distance from the crater.
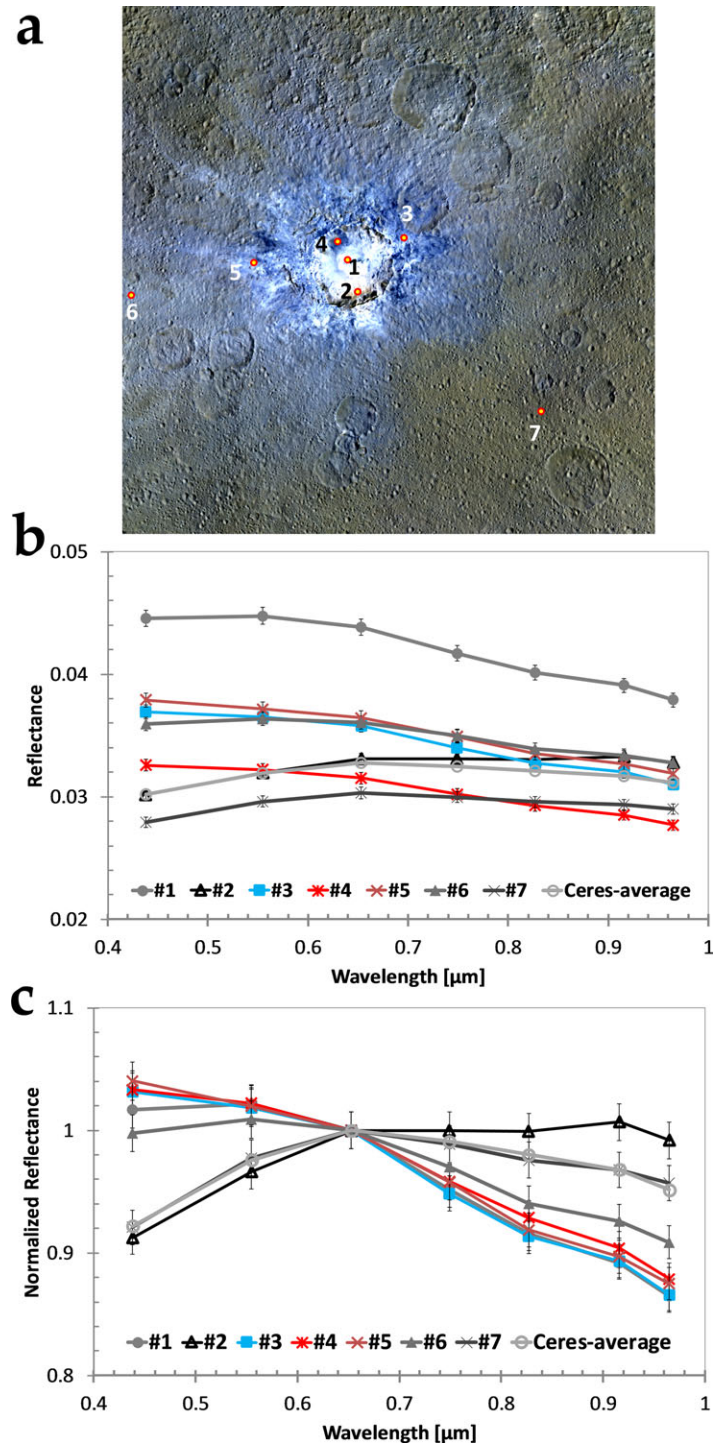
Fig. 3. a) Location of the seven regions of interest (ROIs) used to extract FC color data. Each ROI is made up by 4 × 4 pixels (i.e., a total of 16 pixels) and samples different locations inside crater Haulani and in its neighborhood. b) FC spectra derived in the overall range 0.44–0.96 µm, sampled in seven narrow-band filters. Different colors and symbols refer to the different ROIs marked in (a). An average spectrum of Ceres (light gray line with empty circle points), taken from Thangjam et al. (2018), is also shown for reference. c) Same FC spectra of (b), normalized at 0.65 µm in order to enhance spectral slopes in the visual range. (Color figure can be viewed at wileyonlinelibrary.com.)

Table 1. Summary of the values measured on the basis of FC color data in the seven regions of interest (ROI) considered in Fig. 3a. For each ROI, we list the values of the ratios used in the "Clementine" color code and the values used in the "enhanced" color composite.

	ROI #1	ROI #2	ROI #3	ROI #4	ROI #5	ROI #6	ROI #7
Clementine-*RGB*							
R: 0.75/0.44	0.9358	1.0960	0.9199	0.9280	0.9208	0.9727	1.0741
G: 0.75/0.92	1.0669	0.9934	1.0618	1.0602	1.0679	1.0480	1.0219
B: 0.44/0.75	1.0686	0.9124	1.0872	1.0779	1.0861	1.0281	0.9312
Enhanced-*RGB*							
R: 0.96	0.0379	0.0328	0.0310	0.0277	0.0319	0.0328	0.0290
G: 0.75	0.0417	0.0331	0.0340	0.0302	0.0349	0.0350	0.0300
B: 0.44	0.0446	0.0302	0.0369	0.0326	0.0379	0.0360	0.0279

Table 2. Summary of the FC color data obtained in the seven regions of interest (ROI) considered in Fig. 3a. For each ROI, we list all of the values recorded in the seven narrow-band filters covering the overall spectral range from 0.44 to 096 μm. These measurements were put together to build the FC spectra displayed in Fig. 3b (absolute values) and Fig. 3c (normalized at 0.65 μm), respectively.

Wavelength (μm)	ROI #1	ROI #2	ROI #3	ROI #4	ROI #4	ROI #6	ROI #7
0.44	0.045	0.030	0.037	0.033	0.038	0.036	0.028
0.55	0.045	0.032	0.036	0.032	0.037	0.036	0.030
0.65	0.044	0.033	0.036	0.032	0.036	0.036	0.030
0.75	0.042	0.033	0.034	0.030	0.035	0.035	0.030
0.83	0.040	0.033	0.033	0.029	0.033	0.034	0.030
0.92	0.039	0.033	0.032	0.029	0.033	0.033	0.029
0.96	0.038	0.033	0.031	0.028	0.032	0.033	0.029

The map of visual spectral slope, calculated between 0.555 and 0.829 μm (Fig. 2e), reveals that Haulani stands out for its reduced or even negative values of spectral slope, especially in part of its floor and ejecta (Stephan et al. 2017). In moving away from the crater, the value of the spectral slope gradually decreases to background levels. The lowest values (down to −0.03) are recorded in the central mountainous ridge, western and northwestern inner wall, and in the ejecta closer to the rim, while the southeastern inner wall, as well as some minor localized patches in the eastern, northern, and northeastern inner walls close to the rim, display a positive spectral slope.

Finally, Fig. 2f is a portion of the digital terrain model (DTM) of Ceres for the region of crater Haulani, where the color palette reflects the local topography (Preusker et al. 2016). The maximum topographic relief that occurs in this area is ~6.9 km. The available data sets permit investigation of possible correlations between variations in reflectance, color and mineralogy, and the presence of hills and depressions. The topographic map also serves as a monitoring tool, allowing one to determine whether an observed variation in spectral indices is reliable and not simply due to the combination of local topography and instantaneous solar illumination (see the Tools and Techniques section).

In addition to the maps shown in Fig. 2, we selected seven ROIs within the area where our study focuses. Every ROIs is made up of 4 × 4 pixels, i.e., a total of 16 pixels. For each of these ROIs, we extracted the corresponding FC spectra, measured in seven narrow-band filters from 0.44 to 0.96 μm. Figure 3a shows the locations of these ROIs superimposed on the enhanced color composite map displayed in Fig. 2d; Fig. 3b shows their absolute spectra and Fig. 3c shows the same spectra normalized at 0.65 μm. An average spectrum of Ceres (light gray line with empty circle points), taken from Thangjam et al. (2018), is also shown for reference. Table 1 summarizes the values of the "Clementine" ratios and the *RGB* variables used to build the enhanced color composite of these seven regions. Table 2 summarizes the numeric values measured, for each spectrum, in all of the seven filters.

The brightest point in crater Haulani turns out to be its central mound, corresponding to ROI #1. ROI #7, which is located in the brownish region roughly 80 km southeast of the crater, well approximates the average reflectance of Ceres. The analysis of normalized

spectra in Fig. 3c shows that the ROIs #3 and #5, corresponding to relatively bright ejecta extending respectively to the northeast and west of the crater at short distance from the rim, and ROI #4 which instead refers to a dark material unit in the northwestern inner wall, are those points displaying the bluest spectral slope. The central mound corresponding to ROI #1 is also blue, but less than ROI #3, #4, and #5, despite its higher reflectance. ROI #6 samples ejecta of Haulani located roughly 70 km west of the crater, close to the prime meridian of Ceres. These ejecta, extending into the adjacent quadrangle Ac-H-10 "Rongo," still appear bluish in both the "Clementine" and the "enhanced" maps, although with much more nuanced shade. They display an intermediate reflectance between bright and dark material units found in this region, and their spectral slope is also intermediate between blue units and the average slope of Ceres. On the other hand, ROI #2 and #7, located respectively in the southeastern inner wall and in the region southeast of crater Haulani, are the locations that show the highest spectral slope values (in particular, ROI #7 has a spectral slope that almost perfectly matches the global average slope of Ceres).

FC spectral variations among the bright material units found on Ceres are discussed in detail in Thangjam et al. (2018). All of the bright materials display similar properties at visual wavelengths (peak reflectance at 0.44 or 0.55 μm and blue slope at longer wavelengths); however, variations in the spectral slope and absolute reflectivity are common. In general, the spectral appearance and diversity recorded between the blue-sloped units and the red-sloped units could be of compositional and/or physical property effect.

1.2 and 1.9 μm Reflectances

1.2 and 1.9 μm turn out to be good wavelengths to sample the spectral continuum in the near-infrared, because they are not affected by spectral signatures known or expected to occur on Ceres, as well as by systematic VIR instrumental artifacts. Reflectance maps obtained in the near-infrared at 1.2 and 1.9 μm, with the method briefly addressed in the Tools and Techniques section (Fig. 4), are consistent with the reflectance map obtained by FC in the visual range and confirm that the floor and ejecta of crater Haulani are a patchwork of inherently bright and dark material units.

In particular, the highest reflectance values (~0.04–0.05 at both 1.2 and 1.9 μm) are recorded in the southern floor of the crater, southern inner wall, as well as in the western inner wall and in the ejecta that stretch to the south, while relatively dark material units at these wavelengths (reflectance ~0.02–0.03) are found in the northwestern inner wall and floor, in the ejecta

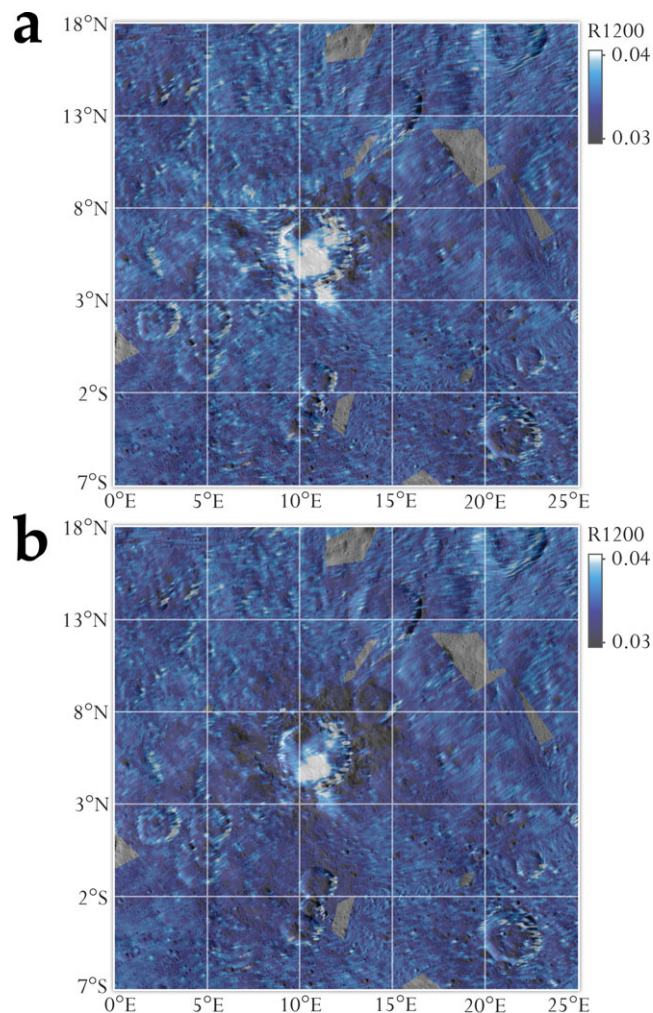Fig. 4. a) Reflectance map of crater Haulani, obtained through photometric correction of VIR data acquired at 1.2 μm in the Survey and HAMO mission phases, interpolated on a grid with a fixed resolution of 40 px/deg, photometrically corrected by using the method described by Ciarniello et al. (2017), i.e., a Hapke photometric correction to standard observation geometry ($i = 30°$, $e = 0°$, $\alpha = 30°$). b) Same map as above, obtained at 1.9 μm. The same photometric correction of (a) was applied. (Color figure can be viewed at wileyonlinelibrary.com.)

that extend toward the east, southeast, and northeast directions in the vicinity of the crater's rim, and in some proximal ejecta that extends to the west. On the large asteroid Vesta, which was the previous target of the Dawn mission, impact craters typically expose layers of both dark and bright material. In that case, the bright layers correspond to fresh pyroxenes processed by relatively little space weathering (McCord et al. 2012; Zambon et al. 2016). Conversely, bright spots on Ceres are thought to be the result of phenomena like cryovolcanism (Ruesch et al. 2016; Russell et al. 2016; Zambon et al. 2017a) and postimpact hydrothermal

activity (Bowling et al. 2016). The bright material units connected to crater Haulani, in addition to being an indicator of their youth, definitely fit in the latter formation scenario.

Near-Infrared Spectral Slopes

The two spectral slopes computed on the basis of VIR data in the near-infrared range—1.163–1.891 µm (Slope 1) and 1.891–2.250 µm (Slope 2) (Fig. 5)—are correlated in space with the spectral slope obtained by FC in the visual range 0.555–0.829 µm at higher spatial resolution (Fig. 2e), i.e., it is confirmed that crater Haulani generally corresponds to a substantial reduction in spectral slope values, with substantial negative values (down to −0.10 and −0.07, respectively) found in the middle of its floor, the western inner wall, and the ejecta closer to the rim, while mass-wasting material found in the southeastern inner wall shows positive values of spectral slope similar to those measured far away from Haulani (Stephan et al. 2017).

Variable spatial correlation in the spectral slopes between the visual range highlighted in the high-resolution FC mosaic (Fig. 2e) and VIR mosaics highlighted in Fig. 5 (i.e., local trends of spectral slopes in the visual range which seem to be neutral in the near-infrared) is due to the fact that, with increasing infrared wavelength, the blue spectral slope recorded in specific Haulani's material units tends to fade and become flatter. It is hard to believe that this slope variation is due to space weathering effects, which should be marginal for a crater as young as Haulani (<6 Myr). Therefore, the observed slope variations are more likely related to other causes such as composition, desiccation, grain size, or a combination of them. Physical alteration such as amorphization and aggregation of small-grained phyllosilicate-rich material and even heating up and melting the impacted surface material to moderate temperatures is expected in the case of low-velocity impact events, which could explain the observed blue spectral slope (Stephan et al. 2017). On Ceres, craters with bright and blue ejecta that show evidence for flows as seen in the "enhanced" color composite maps, like Haulani, may in fact be physically smooth.

2.7 and 3.1 µm Band Depths

Figure 6 reveals a map of the BDs at 2.7 and 3.1 µm (hereafter BD27 and BD31) values measured across the region of crater Haulani. The typical uncertainties associated with the computation of BD27 and BD31 in VIR data are 0.00074 and 0.0069, respectively. A comparison with the topographic map shown in Fig. 2f reveals that the BD in most cases
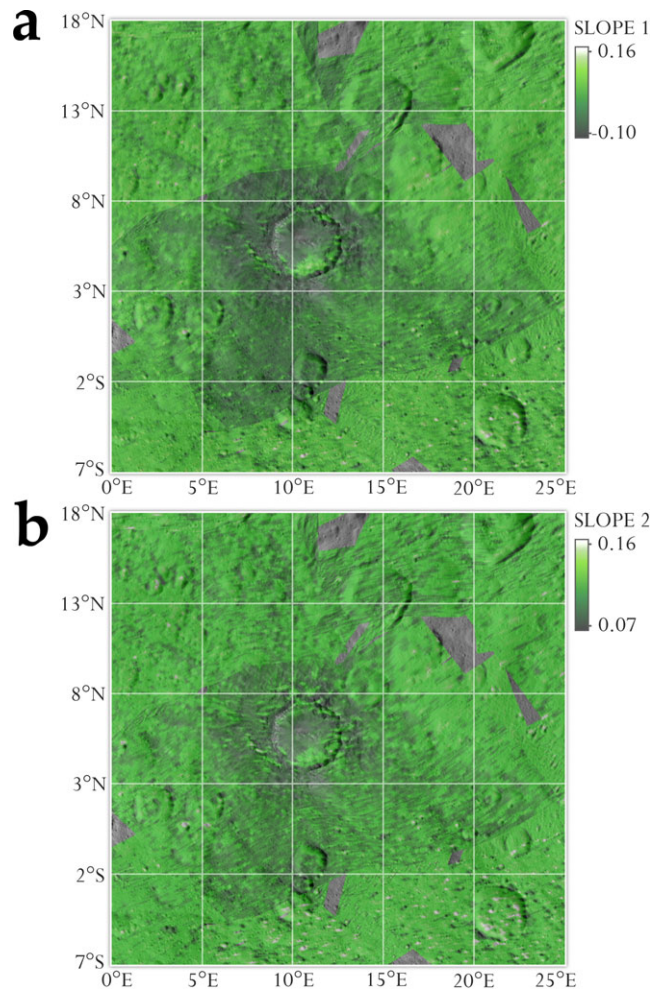

Fig. 5. Two spectral slopes, calculated in the near-infrared range 1.163–1.891 µm (a) and 1.891–2.250 µm (b) on the basis of VIR infrared data. These spectral slopes are essentially consistent with the spectral slope obtained from FC data in the visual range 0.555–0.829 µm at higher spatial resolution (Fig. 2e); i.e., it is confirmed that crater Haulani generally corresponds to a neat reduction in spectral slopes, with negative values found in the middle of its floor, the western inner wall, and the ejecta closer to the rim. (Color figure can be viewed at wileyonlinelibrary.com.)

does not follow the trend of the topography, suggesting that our photometric correction properly removes the effects of topographic slope. The most striking result is that very low BD27 and BD31 values are associated with crater Haulani's floor and ejecta, which appear bluish in FC-derived maps in both the Clementine and enhanced presentations. Exceptions are the southeastern inner wall of the crater and, to a lesser extent, the northeastern rim. This evidence indicates an overall decrease in the abundance of Mg- and NH_4-bearing phyllosilicates in the region of crater Haulani, compared to the surrounding terrains and geologic units.
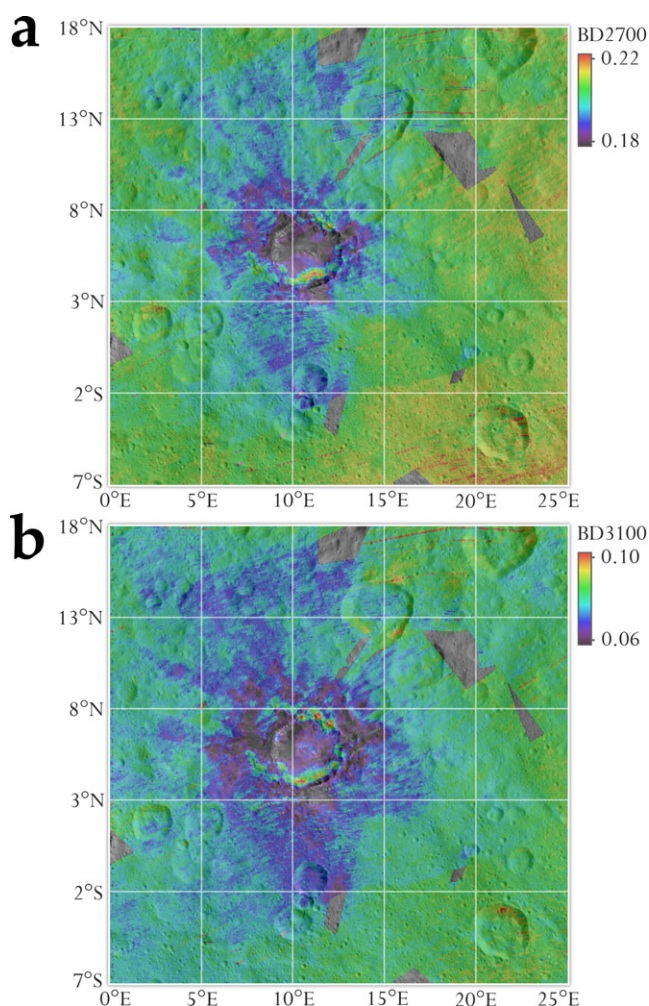
Fig. 6. Distribution of 2.7 μm band depth (BD27) (a) and 3.1 μm band depth (BD31) (b) values across the Haulani quadrangle, derived from VIR data. These band depths are sensitive to the abundance of magnesium-bearing phyllosilicates and ammoniated phyllosilicates, respectively, and to the presence of opaque contaminants. The overall distribution spans from lower depth (violet to blue) to greater depth (red). The floor and ejecta associated with the spectrally distinct material of crater Haulani have shallower BD27 and BD31 values. Substantial spectral variability is recorded in the interior of crater Haulani itself: BD values are shallower on the floor and stronger in the southeastern and northern walls. (Color figure can be viewed at wileyonlinelibrary.com.)

Tosi et al. (2017) pointed out that the spatial correlation in the depth of these two bands is high across crater Haulani, i.e., there is a simultaneous substantial decrease (but not the disappearance) of both Mg- and NH$_4$-bearing phyllosilicates especially in the crater's floor and in the nearest ejecta, while at increasing distances from the crater, the correlation between the BDs (hinting to correlation in the abundances) is much weaker.

4.0 μm Band Center and Band Depth

The mineralogic mapping of carbonates across the entire surface of Ceres is addressed in Carrozzo et al. (2018). One substantial result is that on Ceres the signature of carbonates is usually centered at 3.95 μm, i.e., indicative of Mg- or (Mg,Ca)-rich carbonates, except in specific regions, including crater Haulani. Figure 7 is a closeup of the global map of Carrozzo et al. (2018), revealing the distribution of carbonates in the region of crater Haulani. The typical uncertainties associated with the computation of the BC and BD at 4.0 μm in VIR data are 0.013 and 0.008, respectively.

In its western inner wall, its western rim, and some ejecta that propagate toward the west and northwest, the BC of the spectral feature diagnostic of carbonates moves to longer wavelengths (up to 3.97 μm), indicating the presence of Ca-rich carbonates or a mixture of Mg- and Na-rich carbonate endmembers in the mineralogy of those areas (Palomba et al. 2017).

The map of carbonate BD (Fig. 7b), where each depth value is calculated from the corresponding BC (Fig. 7a), shows that the largest concentration of carbonate minerals is in the western inner wall and the northwestern rim of the crater, plus two patches located just outside of the southern and eastern rims, respectively.

From a direct comparison of the maps shown in Figs. 6 and 7 one can deduce that, in general, the lower abundance of phyllosilicates found in crater Haulani corresponds to a mineralogical variation of carbonates, with Ca- and Na-carbonates showing up and Mg-carbonates that instead dominate the average spectrum of Ceres. At the same time, those areas of the crater that retain a spectral similarity with distant, older terrains (revealed, e.g., by a neutral or positive spectral slope), namely the southeastern inner wall and part of the northern inner wall, also maintain the spectral signature of Mg- or (Mg,Ca)-carbonates typical of the rest of the surface.

However, not necessarily an increase in the abundance of Ca- and Na-rich carbonates corresponds to a decrease in the abundance of phyllosilicates everywhere. Such an anticorrelation exists in the western inner wall and in the western rim, as well as in the western and southern ejecta, but it is weaker in the northeastern rim. In general, any correlation should be investigated and interpreted on a case-by-case basis for specific sites of interest in and around Haulani.

Because the formation of CO$_3$-rich minerals requires relatively high temperatures in a H$_2$O-rich environment, and Ca- and Na-rich carbonates are currently found in the walls, rim, and ejecta of crater Haulani, the likely scenario is their formation in the interior by hydrothermal processes as described in De Sanctis et al. (2016) and Carrozzo et al. (2018),
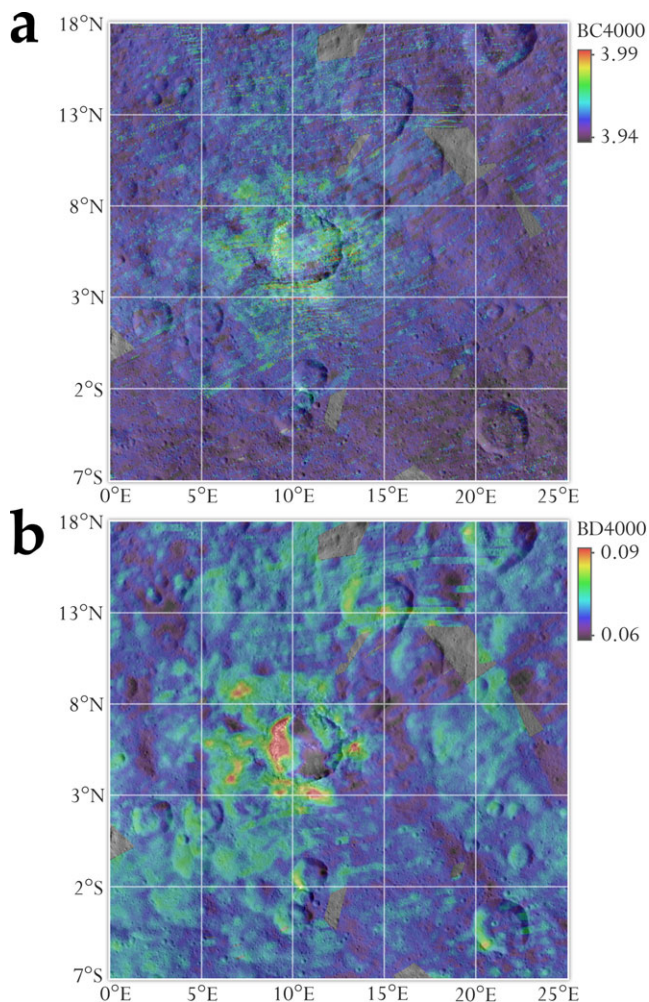
Fig. 7. Distribution of 4.0 μm's band center (a) and band depth (b) values across the region of crater Haulani, derived from VIR data. These parameters are, respectively, sensitive to the composition and abundance of carbonate minerals. The overall distribution spans from Mg- or (Mg,Ca)-rich carbonates (violet to blue) to Na-rich carbonates (red) (a), and from lower depth (violet to blue) to greater depth (red) (b). The western and northwestern inner wall, the eastern inner wall and their respective rims, part of the floor, as well as part of the ejecta, appear enriched in Ca- and Na-rich carbonates compared to surrounding regions. (Color figure can be viewed at wileyonlinelibrary.com.)

triggered by an impact that occurred less than 6 Myr ago. These carbonates are related to brighter material units, similar to what has been observed in several tens of other specific places on Ceres, most notably in crater Occator and in Ahuna Mons (De Sanctis et al. 2016; Palomba et al. 2017; Zambon et al. 2017a, 2017b).

Surface Temperature

Crater Haulani shows the most distinct thermal signature on Ceres, which was first noticed in VIR data acquired in the Approach phase at coarse spatial resolution (11.4 km/px) and under a solar phase angle of 44.5°, covering a substantial fraction of the dayside of Ceres (Tosi et al. 2015a). The region of crater Haulani showed a distinct thermal contrast, being ~5 K cooler than the rest of the surface as observed at 11 h local solar time (LST; Tosi et al. 2015a). The spatial scale of those data could safely rule out shading effects due to local topography. Figure 8 shows VIR-derived temperature values of crater Haulani obtained later in HAMO, in the local cerean morning between 9.0 and 11.3 h LST, in most cases can be explained by instantaneous solar illumination combined with the local topography. However, they reveal that the prominent thermal contrast observed in the early stages of the Dawn mission at Ceres does not arise in the pitted part of the floor (Sizemore et al. 2017), but rather in the central mountainous ridge and possibly in the ejecta closer to the rim, matching bright material with the bluest spectral slope.

Ceres is expected to have a low thermal inertia, albeit greater than Vesta's thermal inertia at global and broadly regional scale (Hayne and Aharonson 2015; Titus 2015). Unfortunately, due to its upper limit of sensitivity at ~5 μm, VIR cannot measure nighttime temperatures on Ceres, which would effectively constrain thermal inertia. However, the maximum daytime temperature is also an important constraint, because this maximum value shifts from the local noon to the afternoon as the thermal inertia of the explored area increases. In this regard, VIR data obtained at Haulani in HAMO do not cover the local noon, but span a range of ~2 h in LST in the local morning.

We have chosen one point located in the central mountainous ridge (6.1°N, 10.3°E) and another point located nearby in the crater's western floor (6.0°N, 9.6°E), so as to ensure that both points were covered in the same VIR observation. We selected VIR cube 494731110, acquired on September 5, 2015 at ~9.2 h LST, and VIR cube 495681682, acquired on September 16, 2015 at ~11.2 h LST. The point in the mountainous ridge shows a mean surface temperature value of 198.3 ± 1.6 K at 9.19 LST, increasing up to 208.6 ± 0.8 K at 11.20 LST. The point in the western floor shows a mean surface temperature value of 212.9 ± 0.6 K at 9.17 h LST, increasing up to 225.1 ± 0.3 K at 11.19 h LST. The temperature difference between these two points as observed at ~0.38 km/px is remarkable: 15–16 K, LST being equal.

To test the hypothesis of a higher thermal inertia, we have run the "Rome" thermophysical model (De Sanctis et al. 2010; Capria et al. 2012). In this model, we assumed the following input parameters: Bond albedo 2–4%, specific heat capacity 600 kJ kg^{-1} K^{-1}, surface density 1350 kg m^{-3} (increasing with increasing depth), and
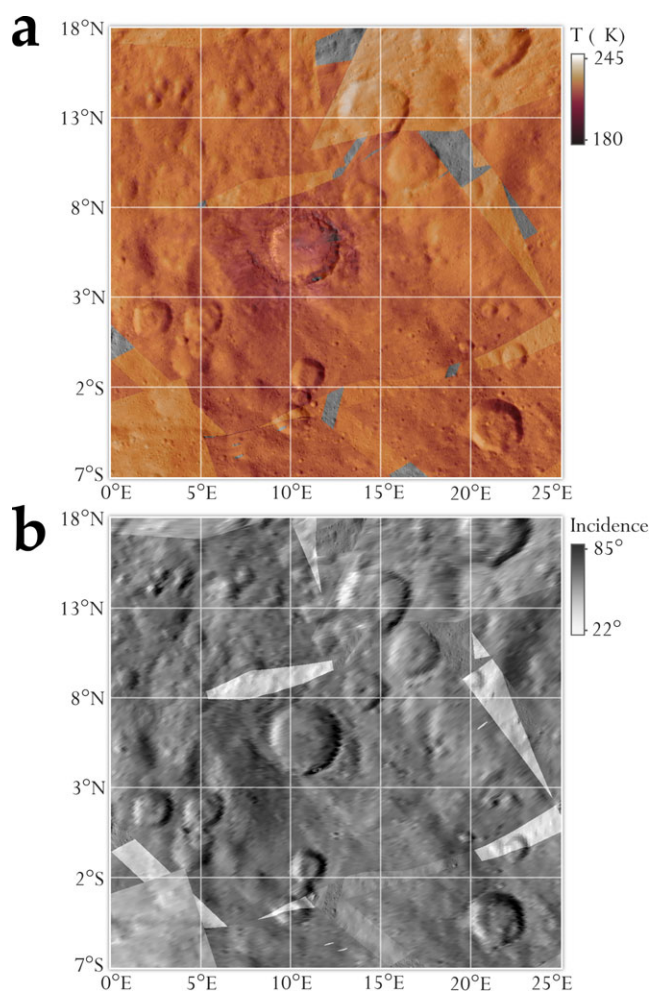
Fig. 8. a) Surface temperature map of crater Haulani, derived from VIR infrared data acquired in the HAMO phase at a spatial resolution of ~0.38 km/px. We adopt a "red temperature" color bar, such that coldest temperatures are shown in the dark red tones while warmest temperatures are whitish. The lower limit (~180 K) is set by the VIR sensitivity range and the rms level of in-flight noise. These observations all occurred in the local cerean morning, at local solar times (LST) between 9.0 and 11.3 h. In this range, surface temperatures are as high as 241 K. b) Map of solar incidence angle of the same region. Surface temperatures recorded in (a) generally follow the local topography, in such a way that areas illuminated at large incidence angles (dark gray to black tones) are cooler than materials illuminated at small incidence angles (light gray to whitish tones). Net changes between shades of gray are due to observations taken at different times under substantially different solar incidence angles (and therefore local solar times). (Color figure can be viewed at wileyonlinelibrary.com.)

thermal conductivity 0.02 W m^{-1} K^{-1} for the central mound and 0.005 W m^{-1} K^{-1} for the floor. Output diurnal temperature profiles display that the thermal behavior of the location in the central mountainous ridge could be fitted by a thermal inertia TIU = 160, which is

double the value of the point located in the crater's floor (TIU = 80). In turn, this value is closer (but still higher) than the global average thermal inertia of Ceres (Fig. 9).

The higher thermal inertia of the central mound of crater Haulani, i.e., its locally slower response to instantaneous insolation compared to the average surface of Ceres, could therefore be the result of brighter, fresh material excavated by the impact combined with a higher thermal conductivity. In this regard, bluish material observed in other surface features on Ceres does not display an equally prominent thermal contrast.

Spectral Unmixing

As anticipated in the Tools and Techniques section, to perform spectral unmixing, we focused on two VIR cubes acquired in the LAMO mission phase, which together embrace more than half of the crater, namely from the middle of its floor to the eastern, northern, and southern rim. Similar to the Survey and HAMO data sets, these LAMO data were previously treated in order to correct both systematic and random instrumental artifacts, remove the thermal emission, apply a photometric correction, and finally display them in equirectangular projection. In general, VIR data obtained in LAMO show a lower SNR than the data acquired in the other mission phases, because they were acquired with larger solar incidence angles (inducing longer shadows in the observed scene), and the VIR footprints are disconnected, due to the high instantaneous speed of the sub-spacecraft point in turn related to the reduced altitude of the spacecraft over the mean surface. These data are also affected by slight smearing effects.

We selected five ROIs, corresponding to as many areas within the Haulani crater, whose locations are shown in Fig. 10 with respect to the equirectangular projection of the VIR data. For each ROI, which is made up by hundreds to thousands of VIR pixels, we tested the result of spectral unmixing by comparing the best fit of the model with the data measured by VIR (Fig. 11). The details of the abundances and other parameters obtained from the model for these five ROIs are summarized in Table 3.

First of all, consistent with the average mineralogy of Ceres, the spectrally featureless dark endmember dominates the composition, being the most abundant component in all cases. In the ROIs under examination, its abundance varies between 56.1 ± 12.8 vol% and 90.1 ± 1.1 vol%, depending on the brighter or darker appearance of the sampled region. Second, within crater Haulani we can safely exclude the presence of water ice (whose abundance is always <1 vol%). This is a
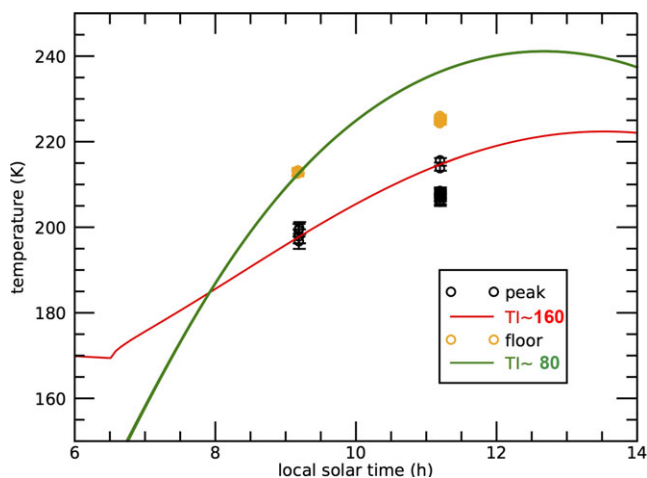
Fig. 9. Theoretical temperature profiles as a function of local solar time obtained by the "Rome" thermophysical model for two points selected inside crater Haulani. The plot is focused on local morning hours where VIR observations are available. VIR-derived temperature measurements for the mound and the floor are represented by the empty black circles and the empty yellow circles, respectively. The green solid line has TIU = 80 and the red solid line has TIU = 160. The red solid line fits the surface temperatures measured by VIR in the local morning, hinting to a substantially higher thermal inertia of the central mound compared to surrounding terrains observed at the same time and under similar solar illumination. (Color figure can be viewed at wileyonlinelibrary.com.)
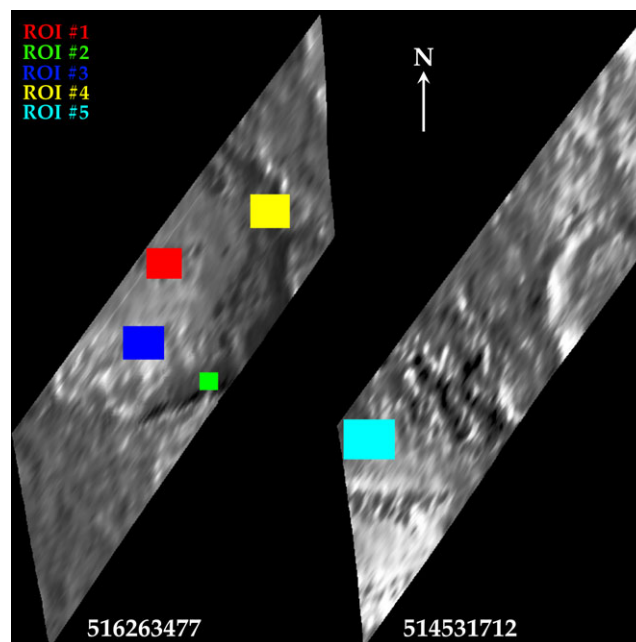

Fig. 10. Equirectangular projection of the two VIR cubes: 516263477 (left), acquired on May 11, 2016 at an average altitude of 376 km, resulting in a pixel resolution of 0.094 km, and 514531712 (right), acquired on April 21, 2016 at an average altitude of 384 km, resulting in a pixel resolution of 0.096 km. In both cases, crater Haulani is only partly covered (north is up). These images together embrace more than half of the crater, namely from the middle of its floor to the eastern, northern, and southern rim, while the western section is out of the field of view. The five different regions of interest (ROIs) considered for our spectral unmixing modeling are marked by boxes with different colors. Each ROI groups hundreds to thousands of VIR pixels (spectra). Distortion in the boundaries of the geologic features (e.g., rim, bright/dark units) arise because VIR footprints here are displayed as connected to each other, whereas gaps actually occur in between them. (Color figure can be viewed at wileyonlinelibrary.com.)

reasonable and predictable result, considering the equatorial latitude of Haulani and its relatively regular shape, which does not allow specific locations to remain in the shadow for long periods during daytime. Anhydrous sodium carbonate or natrite, which is most abundant in the well-known bright spot Cerealia Facula in crater Occator, is absent in all the explored regions, and the same applies to dolomite, which hardly contributes to the spectral fit in most ROIs, whereas hydrous natrite is found in most of the crater's floor and walls, albeit at small concentrations (from 1.2 ± 0.6 vol% to 4.1 ± 1.8 vol%).

We can also exclude a substantial contribution of organic compounds, here represented by kerite, whose abundance, well below the typical values of the organics-rich region close to crater Ernutet (De Sanctis et al. 2017; Pieters et al. 2018), exceeds the detection threshold only in the southeastern inner wall (2.7 ± 1.9 vol%). The same applies to ammonium chloride (maximum abundance 2.7 ± 1.2 vol%). In agreement with the maps of spectral parameters shown in the previous sections, the southeastern inner wall displays the largest abundance of Mg- and NH_4-bearing phyllosilicates, dolomite, and hydrous natrite, while having the smallest grain size (28 μm). Conversely, and also consistent with the maps shown previously,

Haulani's floor (regardless of the considered direction: north, east, or south) is depleted in phyllosilicates, although the grain size is higher on average (93–135 μm). Interestingly, the southern floor shows a nonnegligible abundance of illite (~3.1 ± 0.9 vol%), indicating that aluminum-rich phyllosilicates do not necessarily follow the same trend.

INTEGRATED OBSERVATIONS AND IMPLICATIONS

As documented above and in previous works, the floor and the ejecta of crater Haulani display one of the most negative ("bluest") spectral slopes at visible to near-infrared wavelengths across the entire surface of Ceres. This blue slope is typically associated with bright material units, which is indicative of a younger age and
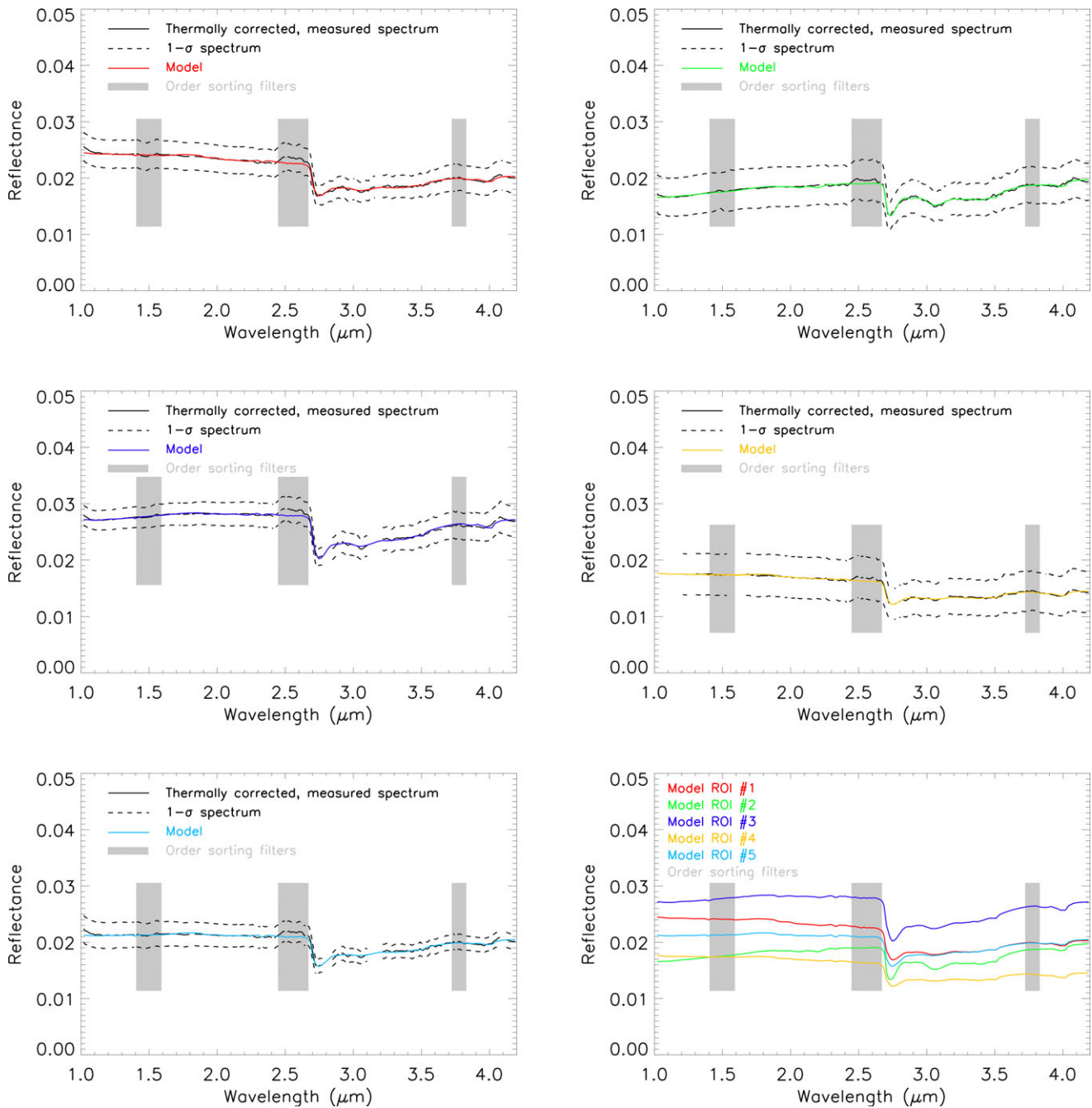
Fig. 11. Graphic result of the spectral unmixing modeling applied to the five different regions of interest selected in Fig. 10. In the various panels, the modeled spectrum is shown as a solid line whose color is consistent with the colors chosen for ROIs of Fig. 10, while VIR measured data are shown in black (the solid line represents the mean spectrum while the dashed lines mark the 1-σ variability). Gray boxes highlight the spectral counterparts (position and width) of three-order sorting filters placed on top of the VIR infrared focal plane, which induce systematic artifacts in the measured data. Finally, the last panel at the bottom right represents a summary of the five modeled spectral profiles together. ROIs #1 and #4, respectively sampling the middle of the floor and the northeastern inner wall, show a blue slope compared to ROI #2, which covers the southeastern inner wall. ROI #3 samples bright material in the southern floor, and ROI #5 samples the northern floor. (Color figure can be viewed at wileyonlinelibrary.com.)

therefore less processed material (Schmedemann et al. 2016; Schröder et al. 2017; Stephan et al. 2017). The bright and bluest materials observed in and around crater Haulani correspond to a decrease in both the BDs of spectral features diagnostic of Mg-bearing and NH$_4$-bearing phyllosilicates, hinting to a substantial

Table 3. Summary of the spectral unmixing modeling obtained for the five regions of interest (ROI) considered within crater Haulani on the basis of VIR data acquired in LAMO. For each ROI, we report the mean values, and associated standard deviations, of the abundances of the 10 spectral endmembers, plus the grain size, required to achieve a best fit with respect to VIR data in the 1.0–4.2 μm spectral range. In all cases, very low abundance values (<1%) bring no meaningful contribution to the fit, and can be considered negligible. When the mean abundance is <1 vol%, the associated uncertainty may be comparable or even greater. In each column, the bold and bold italic, respectively, mark the minimum and maximum values recorded for a given parameter.

	No. of pixels		Kerite	Water ice	Dark	NH4-montmorillonite	NH4Cl	Antigorite	Illite	Dolomite	Natrite	Hydrous natrite	Grain size
ROI #1 (middle floor)	1672	Mean	**0.0015**	0.0006	*0.9010*	0.0218	0.0056	**0.0356**	0.0152	0.0024	0.0020	0.0143	*134.7*
		SD	0.0021	0.0006	0.0109	0.0076	0.0012	0.0062	0.0076	0.0018	0.0035	0.0049	24.0
ROI #2 (SE inner wall)	506	Mean	*0.0270*	*0.0057*	**0.5614**	*0.1415*	*0.0265*	*0.1685*	**0.0097**	*0.0191*	**0.0001**	*0.0405*	**28.4**
		SD	0.0186	0.0059	0.1283	0.0421	0.0115	0.0518	0.0191	0.0175	0.0041	0.0182	30.5
ROI #3 (S floor)	2091	Mean	0.0025	**0.0002**	0.8732	0.0282	**0.0038**	0.0382	*0.0305*	**0.0018**	0.0017	0.0199	93.3
		SD	0.0026	0.0003	0.0168	0.0085	0.0011	0.0071	0.0090	0.0021	0.0034	0.0054	22.7
ROI #4 (NE inner wall)	2058	Mean	0.0027	0.0007	0.8919	**0.0180**	0.0050	0.0390	0.0192	0.0036	*0.0082*	0.0117	130.5
		SD	0.0032	0.0007	0.0168	0.0092	0.0020	0.0096	0.0108	0.0032	0.0104	0.0066	55.7
ROI #5 (N floor)	3200	Mean	0.0009	0.0008	0.8981	0.0172	0.0049	0.0437	0.0183	0.0026	0.0049	**0.0084**	121.3
		SD	0.0015	0.0004	0.0084	0.0053	0.0011	0.0063	0.0075	0.0022	0.0053	0.0045	14.7

References of the spectral endmembers used in this work:
1) Kerite, RELAB sample MA-ATB-043, A. T. Basilevsky, Vernadsky Institute.
2) Water ice (areal mixing), optical constants from: Warren (1984); Mastrapa et al. (2008, 2009); Clark et al. (2012).
3) Magnetite, RELAB sample MG-EAC-002, E. A. Cloutis, University of Winnipeg.
4) NH4-montmorillonite, RELAB sample JB-JLB-189, J. L. Bishop, SETI institute.
5) NH4Cl, RELAB sample CL-EAC-049-A, E. A. Cloutis, University of Winnipeg.
6) Antigorite, RELAB sample AT-TXH-007, T. Hiroi, Brown University.
7) Illite, RELAB sample IL-EAC-001, E. A. Cloutis, University of Winnipeg.
8) Dolomite, RELAB sample CB-EAC-003 E. A. Cloutis, University of Winnipeg.
9) Natrite, RELAB sample CB-EAC-034-C, E. A. Cloutis, University of Winnipeg.
10) Hydrous natrite, RELAB sample CB-EAC-034-A, E. A. Cloutis, University of Winnipeg.

depletion of these mineral species. In the ejecta, this depletion is more prominent in the north–south direction and at relatively short ranges from the crater. The bluish ejecta of Haulani also extend westward, crossing the neighboring quadrangle Ac-H-10 Rongo. In that case, Haulani's ejecta still show depletion in both Mg-bearing and NH_4-bearing phyllosilicates, even though the two BD values show an increasingly weaker correlation with increasing distance from the crater (Tosi et al. 2017; Zambon et al. 2017b).

While no water ice is observed in the region of crater Haulani, and the diagnostic absorptions of Mg-bearing and NH_4-bearing clays are shallower in the crater's floor, implying an overall lower abundance of phyllosilicates, considerable variability in the diagnostic spectral indices used in our work is recorded in the crater as a whole. In particular, the effect of impact processes has not removed or masked the spectral signatures of original mineralogy characteristics of the preimpact event in some specific areas, namely in mass-wasting material found in the southeastern inner wall and some mass-wasting patches located in the northern inner wall close to the rim, which also show a positive spectral slope and an abundance of the main mineral species comparable to the average values recorded farther away. On the other hand, Na- and Ca-rich carbonates found in part of the floor, walls, rim, and ejecta of crater Haulani are most likely a result of the impact event and are related to brighter material units, similar to what has been observed elsewhere on Ceres, most notably in crater Occator and in Ahuna Mons (De Sanctis et al. 2016; Palomba et al. 2017; Zambon et al. 2017a).

An enrichment in carbonates, especially when associated with a lower local content in phyllosilicates, is one evidence in support of intense hydrothermal processes (De Sanctis et al. 2016; Combe et al. 2017). Upwelling, excavation, and exposure of sodium-rich species from depth is observed in several areas of Ceres, including crater Haulani (Carrozzo et al. 2018). The association of Na-carbonates with young craters such as Haulani is consistent with material mobilized or created by impact-induced heating. The correlation of Na-carbonates with some extrusive constructs suggests that at least part of the original Na-carbonate-rich reservoir is exposed to the surface or transported close to the surface by ascending subsurface fluids. Most of the places with Na-carbonates are associated with or close to domes and mounds, like those of Haulani although not exactly superimposed. Craters like Haulani also have fractures on the surface that may be indicative of upwelling processes (Carrozzo et al. 2018).

In this regard, it is worth noting that elsewhere in quadrangle Ac-H-6, other impact craters larger than Haulani do not show the same contrast in terms of mineralogical indices (reflectance, reduced, or even negative spectral slopes; depletion in Mg-bearing and NH_4-bearing phyllosilicates; presence of Na- and/or Ca-rich carbonates) (Tosi et al. 2017). The topographic map of Fig. 2f shows that even in the $25° \times 25°$ region considered for our analysis, the floor of Haulani is less deep than other areas located at relatively short distance both to the east and west of the crater. However, those areas do not display a comparable variability in diagnostic spectral indices, as evidence of the fact that the excavation depth, linked also to the kinetic energy of the impactor, appears of secondary importance compared to the composition of the target area prior to the impact. This supports the hypothesis that initial conditions in terms of shallow subsurface composition may prove crucial in triggering hydrothermal processes, which otherwise would be widespread on the surface. The presence of hydrous natrite albeit in small amounts, along with the absence of natrite, demonstrates that its formation/exposure in Haulani is relatively recent, and dehydration into the anhydrous form Na_2CO_3 is still ongoing.

Because the global mineralogy on Ceres is dominated by a dark, carbonaceous chondrite-like component, Mg- and NH_4-bearing phyllosilicates, and carbonates (De Sanctis et al. 2015, 2018; Ammannito et al. 2016; Carrozzo et al. 2018), one possible explanation is that the projectile that created Haulani could have hit a portion of Ceres originally rich in hydrated (icy) and ammoniated material, penetrating the crust enough to excavate brighter and less processed material and causing intimate mixing between the volatile-depleted regolith and the more volatile-rich material beneath. This scenario is in agreement with the findings of Palomba et al. (2017), who pointed out that Haulani's bright material units may represent an intermediate case between bright spots found in crater Occator (showing very strong carbonate bands, combined with strong metal-OH feature and suppressed ammoniated phyllosilicates feature) or in crater Oxo (showing very strong carbonate bands, and both the ammoniated phyllosilicates and the metal-OH features), and numerous other bright spots found elsewhere on Ceres, showing lower reflectance, shallower carbonate bands, and no substantial depletion in both OH-bearing and NH_4-bearing phyllosilicates. Furthermore, it is also consistent with the evidence that part of crater Haulani's floor is pitted terrain, which on Ceres likely formed via the rapid volatilization of molecular H_2O (probably water ice) entrained in shallow subsurface materials (Sizemore et al. 2017).

The blue-sloped material is the youngest material on Ceres's surface, and the association of flow features with impact craters could be an indication for highly

fluidized material/impact melt (Stephan et al. 2017). Because the shallow subsurface of Ceres harbors water ice (Prettyman et al. 2017; Schmidt et al. 2017), the ejecta of a fresh crater like Haulani might have been initially a slurry mixture of water, phyllosilicates, and Na-carbonates, perhaps as a consequence of impact melting of subsurface water ice that turned blue after desiccation (Schröder et al. 2017). The physical smoothness of the regolith is consistent with the initial liquid condition. However, hydrated Na-carbonates are unstable on airless surfaces and could dehydrate upon exposure to vacuum and irradiation over relatively short time scales (McCord et al. 2001; Bu et al. 2018; Carrozzo et al. 2018). It has also been suggested that bright spots on Ceres might follow a common evolutionary path: initially, the freshest bright spots would have a composition rich in hydrated Na-carbonates, ammoniated salts, and dark compounds. The dehydration of salts and a weak mixing would drive a gradual loss of water, Na-carbonates, and the addition of Mg-phyllosilicates mixed with dark material (Palomba et al. 2017). Space weathering, in terms of diurnal temperature variations and micrometeoritic impacts forming a regolith layer of fine-grained phyllosilicate dust, may be responsible for the fading of the blue color over time (Stephan et al. 2017).

Crater Haulani displays the most distinct thermal signature on Ceres (Tosi et al. 2015a). The crater area is overall cooler than the surrounding regions observed by VIR under similar illumination conditions. This thermal contrast arises in the central mountainous ridge, matching the brightest material with the bluest spectral slope. This suggests that the central ridge may have a thermal inertia higher than the global average of Ceres. In comparison, bluish material observed in other surface features on Ceres does not display an equally prominent thermal contrast. One explanation bounding mineralogical and thermal evidences is that part of the material that melted during the impact event, particularly in the central ridge and in the northern floor and inner wall, shows coarser grain size compared to surrounding terrains, which would explain the higher thermal inertia observed in specific sites.

CONCLUSIONS

In this paper we have carried out an in-depth analysis of the region of crater Haulani on Ceres, using several spectral indices diagnostic of mineralogy and a surface temperature map, overall indicative of the chemico-physical state of the surface. Once all the available results have been put together, the resulting picture can be summarized as follows:

1. Crater Haulani and its ejecta exhibit a peculiar "blue" visible to near-infrared spectral slope. Bright material units, blue spectral slopes, and distinct color properties as seen in multispectral composite images support its young age (< 6 Myr).

2. The "blue" ejecta of Haulani could be the result of the rapid dessication of a slurry mixture of water, phyllosilicates, and carbonates, which remained smooth at spatial scales well beyond the resolution of the best available optical images.

3. Haulani's floor and ejecta are depleted in both magnesium- and ammonium-bearing phyllosilicates, whereas localized patches of sodium- and calcium-bearing carbonates are identified and mapped. On Ceres, this kind of carbonates is not widespread and is indicative of hydrothermal processes triggered by the impact.

4. By estimating the abundances of a series of minerals representative of the surface mineralogy, we detect small amounts of hydrous natrite in the floor and inner walls. Hydrous natrite is a somehow intermediate product between hydrated sodium carbonate (e.g., natron) and anhydrous sodium carbonate (natrite). This implies that the dehydration process following the impact has not yet been completed, again supporting the young age of Haulani.

5. The preimpact composition of the target in its shallow subsurface (in particular, the abundance of hydrated or icy compounds and carbonates) appears to be the primary factor in driving today's surface mineralogy.

6. The crater is home to a marked thermal signature, observable already at broadly regional scale, which originates mainly in its central mountainous ridge and is probably indicative of a greater thermal inertia of the latter, related to a larger grain size and a greater thermal conductivity of the material exposed by the impact. Unlike Vesta, such a thermal behavior is unique in that it has not been recorded in other likewise young craters or bright spots observed across Ceres.

may be obtained at: https://sbn.psi.edu/pds/resource/dwncvir.html

Editorial Handling—Dr. Harry Y. McSween Jr.

REFERENCES

Adams J. B. 1974. Visible and near-infrared diffuse reflectance spectra of pyroxenes as applied to remote sensing of solid objects in the solar system. *Journal of Geophysical Research* 79:4829–4836. https://doi.org/10.1029/JB079i032p04829.

Ammannito E., De Sanctis M. C., Ciarniello M., Frigeri A., Carrozzo F. G., Combe J.-P., Ehlmann B. L., Marchi S., McSween H. Y., Raponi A., Toplis M. J., Tosi F., Castillo-Rogez J. C., Capaccioni F., Capria M. T., Fonte S., Giardino M., Jaumann R., Longobardo A., Joy S. P., Magni G., McCord T. B., McFadden L. A., Palomba E., Pieters C. M., Polanskey C. A., Rayman M. D., Raymond C. A., Schenk P. M., Zambon F., and Russell C. T. 2016. Distribution of phyllosilicates on the surface of Ceres. *Science* 353:aaf4279.

Binzel R. P., De Meo F., Burt B. J., Cloutis E. A., Rozitis B., Burbine T. H., Campins H., Ellen Clark B., Emery J. P., Hergenrother C. W., Howell E. S., Lauretta D. S., Nolan M. C., Mansfield M., Pietrasz V., Polishook D., and Scheeres D. J. 2015. Spectral slope variations for OSIRIS-REx target Asteroid (101955) Bennu: Possible evidence for a fine-grained regolith equatorial ridge. *Icarus* 256:22–29. https://doi.org/10.1016/j.icarus.2015.04.011.

Bishop J. L., Banin A., Mancinelli R. L., and Klovstad M. R. 2002. Detection of soluble and fixed NH_4^+ in clay minerals by DTA and IR reflectance spectroscopy: A potential tool for planetary surface exploration. *Planetary and Space Science* 50:11–19. https://doi.org/10.1016/S0032-0633(01)00077-0.

Bowling T. J., Ciesla F. J., Marchi S., Davison T. M., Castillo-Rogez J. C., De Sanctis M. C., Raymond C. A., and Russell C. T. 2016. Impact induced heating of Occator crater on asteroid 1 Ceres. LPI Contribution 1903. Houston, Texas: Lunar and Planetary Institute. 2268 p.

Bu C., Rodriguez Lopez G., Dukesa C. A., McFadden L. A., Li J.-Y., and Ruesch O. 2018. Stability of hydrated carbonates on Ceres. *Icarus*. https://doi.org/10.1016/j.icarus.2017.12.036.

Capria M. T., Marchi S., De Sanctis M. C., Coradini A., and Ammannito E. 2012. The activity of main belt comets. *Astronomy & Astrophysics* 537:A71. https://doi.org/10.1051/0004-6361/201117556.

Carli C., Ciarniello M., Capaccioni F., Serventi G., and Sgavetti M. 2014. Spectral variability of plagioclase-mafic mixtures (2): Investigation of the optical constant and retrieved mineral abundance dependence on particle size distribution. *Icarus* 235:207–219. https://doi.org/10.1016/j.icarus.2014.03.022.

Carrozzo F. G., Raponi A., De Sanctis M. C., Ammannito E., Giardino M., D'Aversa E., Fonte S., and Tosi F. 2016. Artifacts reduction in VIR/Dawn data. *Review of Scientific Instruments* 87:124,501. https://doi.org/10.1063/1.4972256.

Carrozzo F. G., De Sanctis M. C., Raponi A., Ammannito E., Castillo-Rogez J. C., Ehlmann B. L., Marchi S., Stein N., Ciarniello M., Tosi F., Capaccioni F., Capria M. T.,

Fonte S., Formisano M., Frigeri A., Giardino M., Longobardo A., Magni G., Palomba E., Zambon F., Raymond C. A., and Russell C. T. 2018. Nature, formation and distribution of carbonates on Ceres. *Science Advances*. 4:e1701645. https://doi.org/10.1126/sciadv.1701645

Chapman C. R. and Salisbury J. W. 1973. Comparisons of meteorite and asteroid spectral reflectivities. *Icarus* 19:507–522. https://doi.org/10.1016/0019-1035(73)90078-X.

Ciarniello M., De Sanctis M. C., Ammannito E., Raponi A., Longobardo A., Palomba E., Carrozzo F. G., Tosi F., Li J.-Y., Schröder S. E., Zambon F., Frigeri A., Fonte S., Giardino M., Pieters C. M., Raymond C. A., and Russell C. T. 2017. Spectrophotometric properties of dwarf planet Ceres from the VIR spectrometer on board the Dawn mission. *Astronomy & Astrophysics* 598:A130. https://doi.org/10.1051/0004-6361/201629490.

Clark R. N. 1999. Chapter 1: Spectroscopy of rocks and minerals, and principles of spectroscopy. In *Manual of remote sensing, volume 3, remote sensing for the Earth sciences*, edited by Rencz A. N. New York: John Wiley and Sons. pp. 3–58.

Clark R. N. and Roush T. L. 1984. Reflectance spectroscopy—Quantitative analysis techniques for remote sensing applications. *Journal of Geophysical Research* 89:6329–6340. https://doi.org/10.1029/JB089iB07p06329.

Clark R. N., Cruikshank D. P., Jaumann R., Brown R. H., Stephan K., Dalle Ore C. M., Eric Livo K., Pearson N., Curchin J. M., Hoefen T. M., Buratti B. J., Filacchione G., Baines K. H., and Nicholson P. D. 2012. The surface composition of Iapetus: Mapping results from Cassini VIMS. *Icarus* 218:831–860. https://doi.org/10.1016/j.icarus.2012.01.008.

Cloutis E. A., Hudon P., Hiroi T., Gaffey M. J., and Mann P. 2012. Spectral reflectance properties of carbonaceous chondrites: 8. "Other" carbonaceous chondrites: CH, ungrouped, polymict, xenolithic inclusions, and R chondrites. *Icarus* 221:984–1001. https://doi.org/10.1016/j.icarus.2012.10.008.

Combe J.-P., McCord T. B., Tosi F., Ammannito E., Carrozzo F. G., De Sanctis M. C., Raponi A., Byrne S., Landis M. E., Hughson K. H. G., Raymond C. A., and Russell C. T. 2016. Detection of local H_2O exposed at the surface of Ceres. *Science* 353:aaf3010. https://doi.org/10.1126/science.aaf3010.

Combe J.-P., Raponi A., Tosi F., De Sanctis M. C., Carrozzo F. G., Zambon F., Ammannito E., Hughson K. H. G., Nathues A., Hoffmann M., Platz T., Thangjam G., Schorghofer N., Schröder S. E., Byrne S., Landis M. E., Ruesch O., McCord T. B., Johnson K. E., Singh S. M., Raymond C. A., and Russell C. T. 2017. Exposed H_2O-rich areas detected on Ceres with the Dawn Visible and InfraRed mapping spectrometer. *Icarus*. https://doi.org/10.1016/j.icarus.2017.12.008.

Dalla Mura M., Chanussot J., and Plaza A. 2014. An overview on hyperspectral unmixing. http://www-ljk.imag.fr/membres/Faouzi.Triki/projetPbsInverses/Pre/DallaMura_unmixing.pdf

De Sanctis M. C., Lasue J., and Capria M. T. 2010. Seasonal effects on comet nuclei evolution: Activity, internal structure, and dust mantle formation. *The Astronomical Journal* 140:1–13. https://doi.org/10.1088/0004-6256/140/1/1.

De Sanctis M. C., Coradini A., Ammannito E., Filacchione G., Capria M. T., Fonte S., Magni G., Barbis A., Bini A.,

Dami M., Ficai-Veltroni I., Preti G., and the VIR Team. 2011. The VIR spectrometer. *Space Science Reviews* 163:329–369. https://doi.org/10.1007/s11214-010-9668-5.

De Sanctis M. C., Ammannito E., Raponi A., Marchi S., McCord T. B., McSween H. Y., Capaccioni F., Capria M. T., Carrozzo F. G., Ciarniello M., Longobardo A., Tosi F., Fonte S., Formisano M., Frigeri A., Giardino M., Magni G., Palomba E., Turrini D., Zambon F., Combe J.-P., Feldman W., Jaumann R., McFadden L. A., Pieters C. M., Prettyman T., Toplis M., Raymond C. A., and Russell C. T. 2015. Ammoniated phyllosilicates with a likely outer solar system origin on (1) Ceres. *Nature* 528:241–244. https://doi.org/10.1038/nature16172.

De Sanctis M. C., Raponi A., Ammannito E., Ciarniello M., Toplis M. J., McSween H. Y., Castillo-Rogez J. C., Ehlmann B. L., Carrozzo F. G., Marchi S., Tosi F., Zambon F., Capaccioni F., Capria M. T., Fonte S., Formisano M., Frigeri A., Giardino M., Longobardo A., Magni G., Palomba E., McFadden L. A., Pieters C. M., Jaumann R., Schenk P., Mugnuolo R., Raymond C. A., and Russell C. T. 2016. Bright carbonate deposits as evidence of aqueous alteration on (1) Ceres. *Nature* 536:54–57. https://doi.org/10.1038/nature18290.

De Sanctis M. C., Ammannito E., McSween H. Y., Raponi A., Marchi S., Capaccioni F., Capria M. T., Carrozzo F. G., Ciarniello M., Fonte S., Formisano M., Frigeri A., Giardino M., Longobardo A., Magni G., McFadden L. A., Palomba E., Pieters C. M., Tosi F., Zambon F., Raymond C. A., and Russell C. T. 2017. Localized aliphatic organic material on the surface of Ceres. *Science* 355:719–722. https://doi.org/10.1126/science.aaj2305.

De Sanctis M. C., Ammannito E., Carrozzo F. G., Ciarniello M., Giardino M., Frigeri A., Fonte S., McSween H. Y., Raponi A., Tosi F., Zambon F., Raymond C. A., and Russell C. T. 2018. Ceres's global and localized mineralogical composition determined by Dawn's Visible and InfraRed Spectrometer (VIR). *Meteoritics & Planetary Science*. Forthcoming.

Dobigeon N., Altmann Y., Brun N., and Moussaoui S. 2016. Linear and nonlinear unmixing in hyperspectral imaging. http://dobigeon.perso.enseeiht.fr/papers/Dobigeon_ELSEVIER_2016.pdf

Ehlmann B. L., Hodyss R. P., Bristow T. F., Rossmann G. R., Ammannito E., De Sanctis M. C., and Raymond C. A. 2018. Ambient and cold-temperature infrared spectra of ammoniated phyllosilicates and carbonaceous chondrite meteorites relevant to Ceres and other solar system bodies. *Meteoritics & Planetary Science*. Forthcoming.

Hapke B. 1993. *Theory of reflectance and emittance spectroscopy*. Cambridge: Cambridge University Press. https://doi.org/10.1017/cbo9780511524998.

Hapke B. 2012. *Theory of reflectance and emittance spectroscopy*, 2nd ed. Cambridge: Cambridge University Press. https://doi.org/10.1017/cbo9781139025683.

Hayne P. O. and Aharonson O. 2015. Thermal stability of ice on Ceres with rough topography. *Journal of Geophysical Research: Planets* 120:1567–1584. https://doi.org/10.1002/2015JE004887.

Hiesinger H., Marchi S., Schmedemann N., Schenk P., Pasckert J. H., Neesemann A., O'Brien D. P., Kneissl T., Ermakov A. I., Fu R. R., Bland M. T., Nathues A., Platz T., Williams D. A., Jaumann R., Castillo-Rogez J. C., Ruesch O., Schmidt B., Park R. S., Preusker F., Buczkowski D. L., Russell C. T., and Raymond C. A.

2016. Cratering on Ceres: Implications for its crust and evolution. *Science* 353:aaf4758. https://doi.org/10.1126/science.aaf4759.

Krohn K., Jaumann R., Stephan K., Otto K. A., Schmedemann N., Wagner R. J., Matz K.-D., Tosi F., Zambon F., von der Gathen I., Schulzeck F., Schröder S. E., Buczkowski D. L., Hiesinger H., McSween H. Y., Pieters C. M., Preusker F., Roatsch T., Raymond C. A., Russell C. T., and Williams D. A. 2016. Cryogenic flow features on Ceres: Implications for crater-related cryovolcanism. *Geophysical Research Letters* 43:11,994–12,003. https://doi.org/10.1002/2016GL070370.

Krohn K., Jaumann R., Otto K. A., Schulzeck F., Neesemann A., Nass A., Stephan K., Tosi F., Wagner R. J., Zambon F., von der Gathen I., Williams D. A., Buczkowski D. L., De Sanctis M. C., Kersten E., Matz K.-D., Mest S. C., Pieters C. M., Preusker F., Roatsch T., Scully J. E. C., Russell C. T., and Raymond C. A. 2017. The unique geomorphology and structural geology of the Haulani crater of dwarf planet Ceres as revealed by geological mapping of equatorial quadrangle Ac-H-6 Haulani. *Icarus*. https://doi.org/10.1016/j.icarus.2017.09.014.

Li J.-Y., McFadden L. A., Parker J. Wm., Young E. F., Stern S. A., Thomas P. C., Russell C. T., and Sykes M. V. 2006. Photometric analysis of 1 Ceres and surface mapping from HST observations. *Icarus* 182:143–160. https://doi.org/10.1016/j.icarus.2005.12.012.

Li J.-Y., Reddy V., Nathues A., Le Corre L., Izawa M. R. M., Cloutis E. A., Sykes M. V., Carsenty U., Castillo-Rogez J. C., Hoffmann M., Jaumann R., Krohn K., Mottola S., Prettyman T. H., Schaefer M., Schenk P., Schröder S. E., Williams D. A., Smith D. E., Zuber M. T., Konopliv A. S., Park R. S., Raymond C. A., and Russell C. T. 2016. Surface albedo and spectral variability of Ceres. *The Astrophysical Journal Letters* 817:L22. https://doi.org/10.3847/2041-8205/817/2/L22.

Marquardt D. 1963. An algorithm for least-squares estimation of nonlinear parameters. *SIAM Journal of Applied Mathematics* 11:431–441. https://doi.org/10.1137/0111030.

Mastrapa R. M., Bernstein M. P., Sandford S. A., Roush T. L., Cruikshank D. P., and Dalle Ore C. M. 2008. Optical constants of amorphous and crystalline H_2O-ice in the near infrared from 1.1 to 2.6 μm. *Icarus* 197:307–320. https://doi.org/10.1016/j.icarus.2008.04.008.

Mastrapa R. M., Sandford S. A., Roush T. L., Cruikshank D. P., and Dalle Ore C. M. 2009. Optical constants of amorphous and crystalline H_2O-ice: 2.5-22 μm (4000–455 cm^{-1}) optical constants of H_2O-ice. *The Astrophysical Journal* 701:1347–1356. https://doi.org/10.1088/0004-637X/701/2/1347.

McCord T. B., Orlando T. M., Teeter G., Hansen G. B., Sieger M. T., Petrik N. G., and Van Keulen L. 2001. Thermal and radiation stability of the hydrated salt minerals epsomite, mirabilite, and natron under Europa environmental conditions. *Journal of Geophysical Research* 106:3311–3319. https://doi.org/10.1029/2000JE001282.

McCord T. B., Li J.-Y., Combe J.-P., McSween H. Y., Jaumann R., Reddy V., Tosi F., Williams D. A., Blewett D. T., Turrini D., Palomba E., Pieters C. M., De Sanctis M. C., Ammannito E., Capria M. T., Le Corre L., Longobardo A., Nathues A., Mittlefehldt D. W., Schröder S. E., Hiesinger H., Beck A. W., Capaccioni F., Carsenty U., Keller H. U., Denevi B. W., Sunshine J. M., Raymond C. A., and Russell C. T. 2012. Dark material on Vesta

from the infall of carbonaceous volatile-rich material. *Nature* 491:83–86. https://doi.org/10.1038/nature11561

Nathues A., Platz T., Hoffmann M., Thangjam G., Cloutis E. A., Applin D. M., Le Corre L., Reddy V., Mengel K., Protopapa S., Takir D., Preusker F., Schmidt B. E., and Russell C. T. 2017. Oxo Crater on (1) Ceres—Geologic history and the role of water ice. *The Astronomical Journal* 154:84. https://doi.org/10.3847/1538-3881/aa7a04.

O'Brien D. P., Walsh K. J., Morbidelli A., Raymond S. N., and Mandell A. M. 2014. Water delivery and giant impacts in the "Grand Tack" scenario. *Icarus* 239:74–84. https://doi.org/10.1016/j.icarus.2014.05.009.

Palomba E., Longobardo A., De Sanctis M. C., Stein N. T., Ehlmann B., Galiano A., Raponi A., Ciarniello M., Ammannito E., Cloutis E., Carrozzo F. G., Capria M. T., Stephan K., Zambon F., Tosi F., Raymond C. A., and Russell C. T. 2017. Compositional differences among bright spots on the Ceres surface. *Icarus*. https://doi.org/10.1016/j.icarus.2017.09.020.

Pieters C. M., Staid M. I., Fischer E. M., Tompkins S., and He G. 1994. A sharper view of impact craters from Clementine data. *Science* 266:1844–1848. https://doi.org/10.1126/science.266.5192.1844.

Pieters C. M., Nathues A., Thangiam G., Hoffmann M., Platz T., De Sanctis M. C., Ammannito E., Tosi F., Zambon F., Pasckert J. H., Hiesinger H., Jaumann R., Schröder S. E., Matz K.-D., Castillo-Rogez J. C., Ruesch O., McFadden L. A., O'Brien D. P., Sykes M., Raymond C. A., and Russell C. T. 2018. Geologic constraints on the origin of red organic-rich material on Ceres. *Meteoritics & Planetary Science*. https://doi.org/10.1111/maps.13008.

Platz T., Nathues A., Schorghofer N., Preusker F., Mazarico E., Schröder S. E., Byrne S., Kneissl T., Schmedemann N., Combe J.-P., Schäfer M., Thangjam G. S., Hoffmann M., Gutierrez-Marques P., Landis M. E., Dietrich W., Ripken J., Matz K.-D., and Russell C. T. 2016. Surface water-ice deposits in the northern shadowed regions of Ceres. *Nature Astronomy* 1:0007. https://doi.org/10.1038/s41550-016-0007.

Platz T., Nathues A., Sizemore H. G., Crown D. A., Hoffmann M., Schäfer M., Schmedemann N., Kneissl T., Neesemann A., Mest S. C., Buczkowski D. L., Ruesch O., Hughson K. H. G., Nass A., Williams D. A., and Preusker F. 2017. Geological mapping of the Ac-10 Rongo quadrangle of Ceres. *Icarus*. https://doi.org/10.1016/j.icarus.2017.08.001.

Poch O., Pommerol A., Jost B., Carrasco N., Szopa C., and Thomas N. 2016. Sublimation of water ice mixed with silicates and tholins: Evolution of surface texture and reflectance spectra, with implications for comets. *Icarus* 267:154–173. https://doi.org/10. 1016/j.icarus.2015.12.017.

Prettyman T. H., Yamashita N., Toplis M. J., McSween H. Y., Schörghofer N., Marchi S., Feldman W. C., Castillo-Rogez J., Forni O., Lawrence D. J., Ammannito E., Ehlmann B. L., Sizemore H. G., Joy S. P., Polansky C. A., Rayman M. D., Raymond C. A., and Russell C. T. 2017. Extensive water ice within Ceres' aqueously altered regolith: Evidence from nuclear spectroscopy. *Science* 355:55–59. https://doi.org/10.1126/science.aah6765.

Preusker F., Scholten F., Matz K.-D., Elgner S., Jaumann R., Roatsch T., Joy S. P., Polanskey C. A., Raymond C. A., and Russell C. T. 2016. Dawn at Ceres—Shape model and rotational state. 47th Lunar and Planetary Science Conference, The Woodlands, Texas, 21–25 March 2016. LPI Contribution 1903. 1954 p.

Rand R. S., Resmini R. G., and Allen D. W. 2017. Characterizing intimate mixtures of materials in hyperspectral imagery with albedo-based and kernel-based approaches. *Journal of Applied Remote Sensing* 11:016005. https://doi.org/10.1117/1.jrs.11.016005.

Raponi A., De Sanctis M. C., Carrozzo F. G., Ciarniello M., Castillo-Rogez J. C., Ammannito E., Frigeri A., Longobardo A., Palomba E., Tosi F., Zambon F., Raymond C. A., and Russell C. T. 2018a. Mineralogy of Occator crater on Ceres and insight into its evolution from the properties of carbonates, phyllosilicates, and chlorides. *Icarus*. in press. https://doi.org/10.1016/j.icarus.2018.02.001.

Raponi A., De Sanctis M. C., Frigeri A., Ammannito E., Ciarniello M., Formisano M., Combe J.-P., Magni G., Tosi F., Carrozzo F. G., Fonte S., Giardino M., Joy S. P., Polanskey C., Rayman M. D., Capaccioni F., Capria M. T., Longobardo A., Palomba E., Zambon F., Raymond C. A., and Russell C. T. 2018b. DAWN/VIR discovers changes in the amount of water ice on Ceres' surface. *Science Advances*. 4:eaao3757. https://doi.org/10.1126/sciadv.aao3757

Riner M. A. and Lucey P. G. 2012. Spectral effects of space weathering on Mercury: The role of composition and environment. *Geophysical Research Letters* 39:L12201. https://doi.org/10.1029/2012GL052065.

Rivkin A. S., Volquardsen E. L., and Clark B. E. 2006. The surface composition of Ceres: Discovery of carbonates and iron-rich clays. *Icarus* 185:563–567. https://doi.org/10.1016/j.icarus.2006.08.022.

Roatsch T., Kersten E., Matz K.-D., Preusker F., Scholten F., Jaumann R., Raymond C. A., and Russell C. T. 2016. High-resolution Ceres High Altitude Mapping Orbit atlas derived from Dawn Framing Camera images. *Planetary and Space Science* 129:103–107. https://doi.org/10.1016/j.pss.2016.05.011.

Ruesch O., Platz T., Schenk P., McFadden L. A., Castillo-Rogez J. C., Quick L. C., Byrne S., Preusker F., O'Brien D. P., Schmedemann N., Williams D. A., Li J.-Y., Bland M. T., Hiesinger H., Kneissl T., Neesemann A., Schaefer M., Pasckert J. H., Schmidt B. E., Buczkowski D. L., Sykes M. V., Nathues A., Roatsch T., Hoffmann M., Raymond C. A., and Russell C. T. 2016. Cryovolcanism on Ceres. *Science* 353:aaf4286. https://doi.org/10.1126/science.aaf4286.

Russell C. T., Raymond C. A., Ammannito E., Buczkowski D. L., De Sanctis M. C., Hiesinger H., Jaumann R., Konopliv A. S., McSween H. Y., Nathues A., Park R. S., Pieters C. M., Prettyman T. H., McCord T. B., McFadden L. A., Mottola S., Zuber M. T., Joy S. P., Polanskey C., Rayman M. D., Castillo-Rogez J. C., Chi P. J., Combe J.-P., Ermakov A., Fu R. R., Hoffmann M., Jia Y. D., King S. D., Lawrence D. J., Li J.-Y., Marchi S., Preusker F., Roatsch T., Ruesch O., Schenk P., Villarreal M. N., and Yamashita N. 2016. Dawn arrives at Ceres: Exploration of a small, volatile-rich world. *Science* 353:1008–1010. https://doi.org/10.1126/science.aaf4219.

Schmedemann N., Kneissl T., Ivanov B. A., Michael G. G., Wagner R. J., Neukum G., Ruesch O., Hiesinger H., Krohn K., Roatsch T., Preusker F., Sierks H., Jaumann R., Reddy V., Nathues A., Walter S. H. G., Neesemann A., Raymond C. A., and Russell C. T. 2014. The cratering

record, chronology and surface ages of (4) Vesta in comparison to smaller asteroids and the ages of HED meteorites. *Planetary and Space Science* 103:104–130. https://doi.org/10.1016/j.pss.2014.04.004.

Schmedemann N., Kneissl T., Neesemann A., Stephan K., Jaumann R., Krohn K., Michael G. G., Matz K.-D., Otto K. A., Raymond C. A., and Russell C. T. 2016. Timing of optical maturation of recently exposed material on Ceres. *Geophysical Research Letters* 43:11,987–11,993. https://doi.org/10.1002/2016GL071143.

Schmidt B. E., Hughson K. H. G., Chilton H. T., Scully J. E. C., Platz T., Nathues A., Sizemore H., Bland M. T., Byrne S., Marchi S., O'Brien D. P., Schorghofer N., Hiesinger H., Jaumann R., Pasckert J.-H., Lawrence J. D., Buczkowski D. L., Castillo-Rogez J. C., Sykes M. V., Schenk P. M., De Sanctis M. C., Mitri G., Formisano M., Li J.-Y., Reddy V., LeCorre L., Russell C. T., and Raymond C. A. 2017. Geomorphological evidence for ground ice on dwarf planet Ceres. *Nature Geoscience* 10:338–343. https://doi.org/10.1038/ngeo2936.

Schröder S. E., Mottola S., Carsenty U., Ciarniello M., Jaumann R., Li J.-Y., Longobardo A., Palmer E., Pieters C. M., Preusker F. C., Raymond C. A., and Russell C. T. 2017. Resolved spectrophotometric properties of the Ceres surface from Dawn Framing Camera images. *Icarus* 288:201–225. https://doi.org/10.1016/j.icarus.2017.01.026.

Sierks H., Keller H. U., Jaumann R., Michalik H., Behnke T., Bubenhagen F., Büttner I., Carsenty U., Christensen U., Enge R., Fiethe B., Gutiérrez-Marqués P., Hartwig H., Krüger H., Kühne W., Maue T., Mottola S., Nathues A., Reiche K.-U., Richards M. L., Roatsch T., Schröder S. E., Szemerey I., and Tschentscher M. 2011. The Dawn Framing Camera. *Space Science Reviews* 163:263–327. https://doi.org/10.1007/s11214-011-9745-4.

Sizemore H. G., Platz T., Schorghofer N., Prettyman T. H., De Sanctis M. C., Crown D. A., Schmedemann N., Neesemann A., Kneissl T., Marchi S., Schenk P. M., Bland M. T., Schmidt B. H., Hughson K. H. G., Tosi F., Zambon F., Mest S. C., Yingst R. A., Williams D. A., Russell C. T., and Raymond C. A. 2017. Pitted terrains on (1) Ceres and implications for shallow subsurface volatile distribution. *Geophysical Research Letters* 44:6570–6578. https://doi.org/10.1002/2017GL073970.

Stephan K., Jaumann R., Krohn K., Schmedemann N., Zambon F., Tosi F., Carrozzo F. G., McFadden L. A., Otto K., De Sanctis M. C., Ammannito E., Matz K.-D., Roatsch T., Preusker F., Raymond C. A., and Russell C. T. 2017. An investigation of the bluish material on Ceres. *Geophysical Research Letters* 44:1660–1668. https://doi.org/10.1002/2016GL071652.

Thangjam G., Nathues A., Platz T., Hoffmann M., Cloutis E. A., Mengel K., Izawa M. R. M., and Applin D. M. 2018. Spectral properties and geology of bright and dark material on dwarf planet Ceres. *Meteoritics & Planetary Science*. this issue. https://doi.org/10.1111/maps.13044.

Titus T. N. 2015. Ceres: Predictions for near-surface water ice stability and implications for plume generating processes. *Geophysical Research Letters* 42:2130–2136. https://doi.org/10.1002/2015GL063240.

Tosi F., Capria M. T., De Sanctis M. C., Combe J.-P., Zambon F., Nathues A., Schröder S. E., Li J.-Y., Palomba E., Longobardo A., Blewett D. T., Denevi B. W., Palmer E., Capaccioni F., Ammannito E., Titus T. N., Mittlefehldt D. W., Sunshine J. M., Russell C. T., Raymond C. A., and the Dawn/VIR Team. 2014. Thermal measurements of dark and bright surface features on Vesta as derived from Dawn/VIR. *Icarus* 240:36–57. https://doi.org/10.1016/j.icarus.2014.03.017.

Tosi F., Frigeri A., Combe J.-P., Zambon F., De Sanctis M. C., Ammannito E., Longobardo A., Hoffmann M., Nathues A., Garry W. B., Blewett D. T., Pieters C. M., Palomba E., Stephan K., McFadden L. A., McSween H. Y., Russell C. T., Raymond C. A., and the Dawn Science Team. 2015a. Mineralogical analysis of the Oppia quadrangle of asteroid (4) Vesta: Evidence for occurrence of moderate-reflectance hydrated minerals. *Icarus* 259:129–149. https://doi.org/10.1016/j.icarus.2015.05.018.

Tosi F., De Sanctis M. C., Zambon F., Ammannito E., Capria M. T., Carrozzo F. G., Li J.-Y., Longobardo A., Mottola S., Palomba E., Raponi A., Raymond C. A., and Russell C. T. 2015b. Preliminary temperature maps of dwarf planet Ceres as derived by Dawn/VIR. European Planetary Science Congress 2015, 27 September-2 October 2015, Nantes (France). ADS Bibcode: 2015EPSC...10..281T.

Tosi F., Carrozzo F. G., Zambon F., Ciarniello M., Frigeri A., Combe J.-P., De Sanctis M. C., Hoffmann M., Longobardo A., Nathues A., Raponi A., Thangjam G., Ammannito E., Krohn K., McFadden L. A., Palomba E., Pieters C. M., Stephan K., Raymond C. A., Russell C. T., and the Dawn Science Team. 2017. Mineralogical analysis of the Ac-H-6 Haulani quadrangle of the dwarf planet Ceres. *Icarus*. in press. https://doi.org/10.1016/j.icarus.2017.08.012.

Warren S. G. 1984. Optical constants of ice from the ultraviolet to the microwave. *Applied Optics* 23:1206–1225. https://doi.org/10.1364/AO.23.001206.

Zambon F., Tosi F., Carli C., De Sanctis M. C., Blewett D. T., Palomba E., Longobardo A., Frigeri A., Ammannito E., Russell C. T., and Raymond C. A. 2016. Lithologic variation within bright material on Vesta revealed by linear spectral unmixing. *Icarus* 272:16–31. https://doi.org/10.1016/j.icarus.2016.01.009.

Zambon F., Raponi A., Tosi F., De Sanctis M. C., McFadden L. A., Carrozzo F. G., Longobardo A., Ciarniello M., Krohn K., Stephan K., Palomba E., Pieters C. M., Ammannito E., Russell C. T., and Raymond C. A. 2017a. Spectral analysis of Ahuna Mons from Dawn mission's visible-infrared spectrometer. *Geophysical Research Letters* 44:97–104. https://doi.org/10.1002/2016GL071303.

Zambon F., Carrozzo F. G., Tosi F., Ciarniello M., Combe J.-P., Frigeri A., De Sanctis M. C., Hoffmann M., Longobardo A., Nathues A., Stephan K., Raponi A., Thangjam G., Ammannito E., Krohn K., McFadden L. A., Palomba E., Raymond C. A., Russell C. T., and the Dawn Science Team. 2017b. Spectral analysis of quadrangle Ac-H-10 Rongo on Ceres. *Icarus*. in press. https://doi.org/10.1016/j.icarus.2017.09.021.